Master's thesis

2020

John Reboli Olsen

NTNU
Norwegian University of
Science and Technology
Faculty of Natural Sciences
Department of Materials Science and Engineering

John Reboli Olsen

A Combined Thermal Cycle Software for Welded and Locally Heat Treated 6082 Aluminium Alloys

July 2020

NTNU
Norwegian University of
Science and Technology

NTNU
Norwegian University of
Science and Technology

NTNU

Norwegian University of
Science and Technology

A Combined Thermal Cycle Software for Welded and Locally Heat Treated 6082 Aluminium Alloys

John Reboli Olsen

Materials Science and Engineering
Submission date: July 2020
Supervisor: Trond Furu
Co-supervisor: Bjørn Holmedal, Ole Runar Myhr

Norwegian University of Science and Technology
Department of Materials Science and Engineering

Abstract

This paper covers the development of a Combined Weld and Induction Thermal Cycle software used to estimate the thermal cycles during welding and local post weld heat treatment, LPWHT, by induction heating of 6082.50-T6 aluminium. The Combined Weld and Induction Thermal Cycle software is developed in MatLab R2017b by implementation of analytical models which describe the thermal cycles of welding and LPWHT. The LPWHT by induction heating aims to manipulate the geometry of the heat affected zone, HAZ, after welding of 6082.50-T6 aluminium structures, to increase the structural properties. Lastly, the thermal cycles are used as input to a precipitation, yield strength and work-hardening software, NaMo, which estimates the resulting mechanical properties after welding and LPWHT.

The developed software was calibrated based on experimental data, from both this study and a preceding one, and shows a good correspondence with the experimental data. The net power for the induction heating was found to 1898 W and the efficiency equal to 0.251, with a discrete partial heat source distribution. Predictions indicate that a manipulation of the HAZ is possible. After welding and LPWHT, followed by a room temperature storage, RT-storage, of 14 days, the predicted lowest hardness in the HAZ has slightly decreased. A post weld heat treatment, PWHT, after welding and LPWHT increased the predicted lowest hardness by between 8.7-31.4 % at the surface, while the predicted lowest hardness at the center of the thickness of the material was slightly reduced. The addition of a PWHT indicates that the methodology of a LPWHT could increase the structural properties of welded 6082.50-T6 aluminium structures.

Sammendrag

Denne oppgaven dekker utviklingen av et kombinert termisk syklus-program for sveising og induksjon, Combined Weld and Induction Thermal Cycle software, som brukes til å estimere de termiske syklusene under sveising og lokal varmebehandling etter sveising, LPWHT, ved induksjonsoppvarming av 6082.50-T6 aluminium. Programmet, Combined Weld and Induction Thermal Cycle software, er utviklet i MatLab R2017b ved implementering av analytiske modeller som beskriver de termiske syklusene for sveising og lokal varmebehandling. Den lokale varmebehandlingen etter sveising har som mål å manipulere geometrien til den varmepåvirkede sonen, HAZ, etter sveising av 6082.50-T6 aluminiumkonstruksjoner, for å øke de strukturelle egenskapene. Til slutt blir de termiske syklusene brukt som input til et program for presipitering, flytespenning og arbeidsherding, NaMo, som estimerer de resulterende mekaniske egenskapene etter sveising og LPWHT.

Det utviklede programmet ble kalibrert basert på eksperimentelle data, både fra denne oppgaven og den foregående, og viser en god overensstemmelse med eksperimentelle data. Nettoeffekten for induksjonsoppvarmingen ble bestemt til 1898 W og virkningsgraden lik 0.251, med en diskret varmekildefordeling. Estimatene gjort av det utviklede programmet og NaMo, indikerer at en manipulering av HAZ er mulig. Etter sveising og LPWHT, fulgt av en romtemperaturlagring, RT-storage, på 14 dager, har den estimerte laveste hardheten i HAZ blitt noe redusert. En varmebehandling etter sveising, PWHT, og LPWHT økte den estimerte laveste hardheten med mellom 8,7-31,4 % ved overflaten, mens den estimerte laveste hardheten i midten av tykkelsen på materialet ble redusert. En varmebehandling etter sveising og LPWHT indikerer at ideen om en LPWHT, kan øke de strukturelle egenskapene til sveisede 6082.50-T6 aluminiumkonstruksjoner.

Preface and Acknowlegdements

This master's thesis is written during the spring semester of 2020 as a part of the MSc degree in Materials Science and Engineering at the Norwegian University of Science and Technology, NTNU, in Trondheim. The project is linked to the NTNU Aluminium Production Innovation Center, NAPIC, Norsk Hydro ASA and SINTEF Manufacturing AS. The presented work is a continuation of the specialization project "Mechanical and Metallurgical Analysis of a Welded and Post-Weld Heat Treated 6082 Aluminium Alloy" completed during the fall semester of 2019. Parts of this project are reused in this thesis.

I want to thank my supervisor, Dr. Trond Furu[1], for his guidance regarding the work presented in this thesis. I would also like to thank my co-supervisors Dr. Ole Runar Myhr[2] and Professor Bjørn Holmedal[3] for their encouragement and help, in addition to helpful feedback during this semester. A thanks is also owed to Senior Research Scientist Rune Østhus[4] for his guidance and support during and after my visit to SINTEF Manufacturing AS at Raufoss.

Lastly, I would like to thank my friends and classmates for making the last five years of studying and not studying in Trondheim the best they could ever have been. The numerous long coffee breaks with discussions about nothing and everything have been very important for both my studies and me.

John Reboli Olsen
Trondheim, July 2020

[1] Norsk Hydro, Sunndalsøra
[2] Norsk Hydro, Raufoss
[3] NTNU, Trondheim
[4] SINTEF Manufacturing, Raufoss

Contents

List of Tables

List of Figures

Abbreviations

AA	=	Artificial aging
AA6xxx	=	6xxx-series aluminium alloys
A	=	Cross section area
F	=	Load by tensile or compressive force
GMAW	=	Gas metal arc welding
GP-zones	=	Metastable Guinier-Preston zones
HAZ	=	Heat affected zone
HV	=	Vickers hardness
LPWHT	=	Local post weld heat treatment
MIG	=	Metal inert gas
NA	=	Natural aging
NaMo	=	Nanostructure Software
O	=	Temper condition of annealed aluminium
SHT	=	Solution heat treatment
SSSS	=	Supersaturated solid solution
T4	=	Temper condition of naturally aged aluminium
T6	=	Temper condition of artificially aged aluminium to peak strength
P	=	Induction output power
P_{net}	=	Net power input from induction
PWHT	=	Post weld heat treatment
RT	=	Room temperature
β	=	Stable phase, Mg_2Si in AA6xxx
β'	=	Strengthening precipitate, Mg_5Si_3 in AA6xxx
β''	=	Strengthening precipitate, Mg_5Si_6 in AA6xxx
σ_{max}	=	Load bearing capacity
σ_y	=	Yield strength
$\sigma_{y,HAZ}$	=	Lowest yield strength of the HAZ
η_{arc}	=	Arc efficiency factor
η_{IND}	=	Induction efficiency factor

Chapter 1

Introduction

1.1 Background

Aluminium is a well established material in many engineering applications. The good strength to weight ratio and relatively good natural corrosion resistance makes it competitive in the construction and automotive industry among others [1]. The strength of certain aluminium alloys can match some construction steels [1], hence the strength to weight ratio is by far superior.

The 6xxx-series of aluminium alloys, AA6xxx, are commonly applied in aluminium extrusion products. The extrusions can be used in a variety of applications from construction material, automotive panels and even in aerospace applications [2, 1]. Welding is a bonding process that can be used to join AA6xxx components. A common welding technique, called Gas Metal Arc Welding, GMAW, utilizes an arc to melt the two components together, often with a filler material [3, 4]. The temperature is elevated incredibly fast above the melting temperature by the arc and upon solidification a metallurgical bond connects the components.

A complex thermal processing route ensures good mechanical properties of the AA6xxx. A process known as precipitation heat treatment gives the most important strength contribution for AA6xxx [1]. During welding of AA6xxx the fine-tuned precipitate structure from the complex thermal processing is altered. A region adjacent to the weld, called the heat affected zone, HAZ, is heavily affected by the heat from the arc. The precipitates in this region can dissolve, grow or remain unaffected, affecting the mechanical properties. Even though AA6xxx are considered to have reasonable weldability, a significant drop in strength is observed for welded AA6xxx, and the strength to weight ratio is compromised [3, 5].

Recovering some of the lost strength in the HAZ is beneficial, as the strength of on the entire component is limited by the strength of the HAZ, thus affecting the weight and hence cost of the welded material. A previous study by Hamarsnes [6] investigated the effect of applying weld strings on the surface of the welded components perpendicularly over the original weld, termed cross-welds, to manipulate the HAZ geometry and affect the global stress on the component under loading. The same study by Hamarsnes and a study by Gjertsen [7] used the same methodology with a laser to manipulate the HAZ. The results from laser heat treatments were somewhat varying, but the cross welds in combination with a post weld heat treatment, PWHT, improved the ultimate tensile strength, UTS, by 47 MPa and fracture strain by 120% [6]. The studies concluded that the original HAZ geometry is altered by and caused stress to localize differently.

The specialization project [8] preceding this thesis investigated the effect of applying a local post weld heat treatment, LPWHT, by induction heating to manipulate the HAZ geomtery. The LPWHT by induction heating showed promising results regarding manipulation of the HAZ geometry. A recent methodology by Østhus et al. [9] simulated the incorporation of the LPWHT by induction heating followed by a PWHT on welded AA6xxx components. The simulations showed promising results regarding global strength recov-

ery, as the predicted maximum applied load after LPWHT and PWHT could be increased by up to 20% [9].

Simulations of thermal processing, like the one presented by Østhus et al. [9], enables estimations to made before extensive experimental testing starts. Predictive models which give reasonable estimates and the software implementation of these models are important building blocks in the study by Østhus et al. [9] among others.

1.2 Objective

The objective of this study was to investigate if the methodology by Østhus et al. [9] could be reproduced and improved primarily by experimental testing. However due to inadequate laboratory access as a result of the outbreak of the Covid-19 virus, the objective had to be reevaluated. The revised objective of this study is to formulate and implement the combined thermal history for welding and LPWHT of the HAZ by induction heating of a 6082.50-T6 aluminium alloy in a software. The thermal history is a key factor in the methodology proposed by Østhus et al. [9].

The experimental testing was started by thermal processing and welding of extruded 6082.50-T6 aluminium alloy sheets. The thermal history during welding and LPWHT is based on analytical models by Rykalin [4, 9, 10]. Calibration of the LPWHT by induction heating software is based on experimental data from the preceding specialization project [8]. The thermal history output from the combined thermal history software will then serve as an input for a combined precipitation, yield strength and work hardening software for AA6xxx called NaMo [11, 12, 13, 14]. NaMo is used to estimate the precipitation and strength evolution due to the thermal processing for a given thermal history of a point in the HAZ provided by the developed combined thermal history software. Comparisons between experimental data and the predictions are made to evaluate the validity of the developed software.

Chapter 2

Theory

This chapter describes the physical-metallurgic theory of aluminium alloys, the welding process and the modification of the HAZ. The models which are used to describe the welding process and modification of the HAZ by LPWHT, are also presented and explained. Lastly, the theory behind the software NaMo is described.

2.1 Aluminium Alloys

Aluminium has a low density of $2.7\,\mathrm{g/cm^3}$ and is a favorable light metal for applications in the automotive industry, aerospace and construction [1, 15]. In its pure form aluminium is very soft, but with addition of alloying elements some aluminium alloys can achieve a higher strength than some steels [1]. The strength to weight ratio of aluminium alloys are generally high, hence aluminium is competitive in a wide range of applications. In addition to the great mechanical properties, aluminium has a natural corrosion resistance [1, 15]. A dense oxide film with low permeability forms spontaneously on the surface protecting from further oxidation (corrosion).

2.1.1 The 6xxx-series of Aluminium Alloys

Aluminium alloys are classified as cast or wrought alloys, and by their chemical composition, as some alloys are heat-treatable and some non-heat-treatable. The strength of heat treatable wrought alloys is a result of precipitation from the alloying elements and cold/hot working [1, 15]. AA6xxx, is a heat treatable series of wrought alloys. The main alloying elements are Mg and Si, typical concentrations are 0.5-1.3 wt% for Mg and 0.4-1.4 wt% for Si. Mn and Cr can be added in small amounts for grain refinement as the elements form dispersoids during homogenization which inhibit recrystallization [16]. A small amount of Cu can be added for increased strength [1].

As the AA6xxx are heat-treatable, the mechanical properties can be easily manipulated and fine-tuned. Table 2.1 lists typical mechanical properties of heat treated AA6xxx. The yield strength, σ_{y}, ultimate tensile strength, σ_{UTS} and percentage elongation are generally high. The yield strength can reach up to about 360 MPa, while the ultimate tensile strength can reach up to about 390 MPa for AA6xxx heat treated to peak strength.

Table 2.1: Typical mechanical properties of different heat treated AA6xxx [1].

σ_{y} [MPa]	σ_{UTS} [MPa]	Elongation [%]
190-360	220-390	12-17

2.1.2 Thermal Processing

Heat treatable wrought aluminium alloys are subject to thermal processing with multiple steps. A typical thermal processing route of extruded and artificially aged AA6xxx is described below and in Figure 2.1. The first thermal processing step after casting is homogenization. The cast aluminium billet is heated to a high temperature, typically 560-600 °C [5]. Heating to this temperature eliminates the solute gradients after casting and room temperature storage, RT-storage [5]. Dispersoids of Mn and Cr form during homogenization [17]. Internal stress from the casting is also relieved during homogenization [5]. The aluminum billet is then cooled to room temperature.

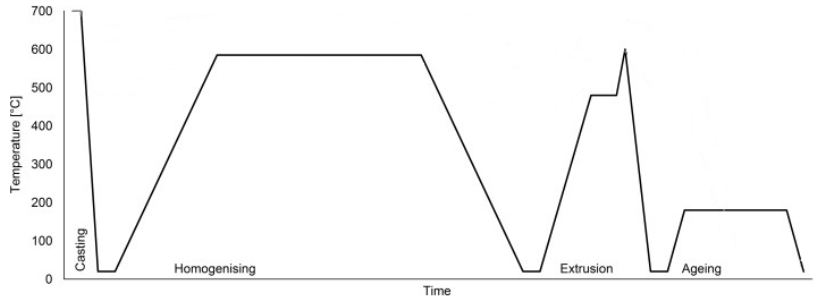

Figure 2.1: Illustration of the thermal history of extruded and artificially aged aluminium. Recreated from [18].

The next step is called extrusion, a thermal processing technique where the aluminium billet is forced through a die by a hydraulic press. The products, extruded profiles, can be made with a specific geometry by selecting a proper die and orifice [5]. After homogenization the billet is preheated to the extrusion temperature. Homogenization and extrusion preheating can be combined, but will not likely produce matching mechanical properties of material produced with homogenization and extrusion as separate steps [5]. The extruded profile will reach solution heat treatment temperature upon leaving the die before cooling to room temperature, hence solution heat treatment, SHT, is often combined with the extrusion in the extrusion press. Cooling medium and hence cooling rate will depend on the alloy and dimensions of the profile, thicker profiles requiring water quenching, while thin profiles may be air quenched [5]. SHT and quenching ensures a supersaturated solid solution, SSSS, before artificial aging, which is critical for artificial aging of heat-treatable aluminium alloys and will be described in the following section [5]. SHT can be repeated before artificial aging if the alloy is left in storage after extrusion.

After SHT and a slight hold-up at RT follows artificial aging, AA, which is a precipitation heat treatment. This step is conducted at lower temperatures, typically in the range 150-200°C, for several hours, before cooling to room temperature [15]. The artificial aging will result in the formation of metastable precipitates from the SSSS, contributing to the strength of the alloy, and will be further described in the next section 2.1.3. Natural aging can also occur for the AA6xxx, and is not a direct thermal processing step, however an important mechanism. Natural aging occurs at ambient temperatures after extrusion and/or SHT from a SSSS. Metastable precipitates (not the same type as for AA) will slowly form if the alloy is left at ambient temperatures for a longer period of time. Naturally aged alloys will not achieve the same strength level as artificially aged ones [5]. Typical solution heat treatment temperatures for the 6082 aluminium alloys, for both the T4 and T6 temper are 535-575°C. A aging temperature of 185°C for 5.5 hours is used to achieve a T6 temper[1].

[1] SINTEF Manufacturing and Norsk Hydro at Raufoss

2.1.3 Precipitation and the Influence of Alloying Elements

Heat treatable aluminium alloys such as the AA6xxx achieve their strength primarily from precipitation hardening [19]. Figure 2.2 depicts the psuedo-binary phase diagram of Al and the equilibrium phase Mg_2Si. For a AA6xxx, the solubility of Mg_2Si in a pure Al matrix is lower at room temperature than at higher temperatures like solution heat treatment temperature. The narrowing single phase area of Al is an indication of the solubility decrease. Hence, more Mg and Si can enter solid solution at higher temperatures. The two-phase area of Al + Mg_2Si indicates that these phases can coexist in a stable manner.

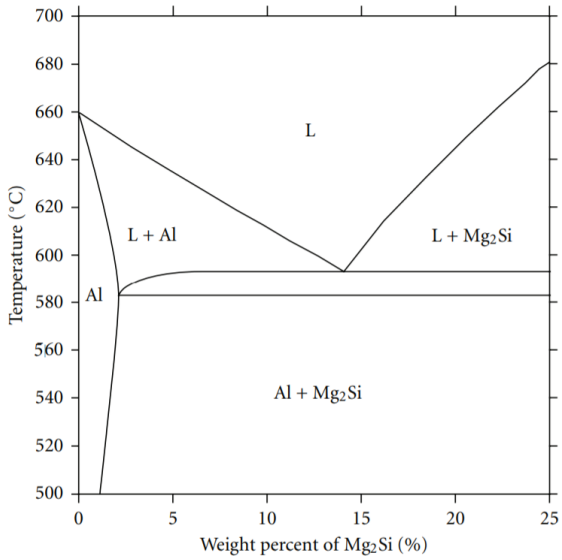

Figure 2.2: Psuedo-binary phase diagram of Al and Mg_2Si. Copied from [20].

A very important conclusion can be made from interpreting the pseudo-binary phase diagram in Figure 2.2. Consider an alloy with composition of Mg_2Si of 2%. The alloy will experience precipitation of Mg_2Si upon cooling from a high temperature, e.g. casting or SHT. Precipitation of Mg_2Si will occur for alloys with compositions of Mg_2Si over about 1%, described by the two phase are of Al + Mg_2Si. If the cooling rate is very high, e.g. by quenching the alloy, the Mg and Si will be trapped in a SSSS in the Al-matrix [5], as the time is not sufficient for diffusion of Mg and Si to occur [15].

If the temperature is elevated, the diffusion rate of the alloying elements will increase [15]. If an alloy in a SSSS state is kept at elevated temperature over time, diffusion of alloying elements and phase transformations will result in formation of metastable precipitates. This mechanism is put to use during artificial aging. From the SSSS, the alloying elements will form clusters. The clusters grow and form Guinier Preston-zones, GP-zones. The GP-zones are partially coherent needles oriented along the $\langle 100 \rangle$-direction. Continued

aging causes the GP-zones to grow into precipitates denoted β''. The β''-precipitates have the chemical composition Mg_5Si_6 and are also partially coherent needles oriented along the $\langle 100 \rangle$-direction. Formation of another type partially coherent rods, β'-precipitates, in the $\langle 100 \rangle$-direction follows. β'-precipitates have chemical composition Mg_5Si_3. The β'-precipitates can coarsen further to the stable phase Mg_2Si called β-precipitates. The precipitation sequence is described by [1]:

$$\text{SSSS} \rightarrow \text{clusters} \rightarrow \text{GP-zones} \rightarrow \beta'' \rightarrow \beta' \rightarrow \beta \tag{2.1}$$

The peak strength, T6 temper, is achieved with a mix of mainly β''-precipitates and some β'-precipitates [21]. The 6082 alloy is especially responsive from the SSSS state. Diffusion will occur even at room temperature and the alloying elements form clusters (and GP-zones). This process is called natural aging, leading to the T4 temper [21]. Figure 2.3 illustrates the strength contribution as a function of aging time during artificial and natural aging for AA6xxx. The T4 and T6 tempers are depicted in Figure 2.3 as well. Overaging is a term for aging longer than T6-temper at elevated temperatures. Upon overaging, coarse β-precipitates will form and the resulting strength is less than for the T6 temper. Fully annealed temper, O, with coarse β-precipitates is seen in Figure 2.3 as well.

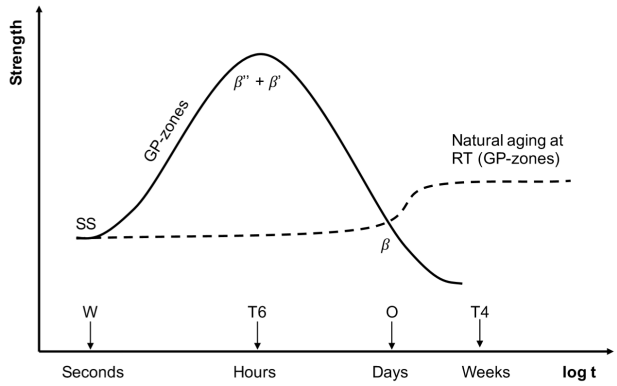

Figure 2.3: Illustration of the precipitation sequence and the strength contribution as a function of aging time during artificial and natural aging for AA6xxx. Copied from [21].

2.1.4 Strengthening Mechanisms

Dislocations allow for plastic deformation in metals, as they move through a metal subject to an externally applied stress exceeding a critical value [15]. The dislocation movement causes the material to ”flow”. The strength of an aluminium alloy is a result of inhibited dislocation movement due to different strengthening mechanisms [15]. Dislocation movement can be inhibited by alloying elements in solid solution, internal defects, such as grain boundaries and other dislocations, and precipitates, both shearable and non-shearable.

The primary strengthening mechanisms of the AA6xxx are solid solution strengthening

and precipitation strengthening [19]. Solid solution strengthening is caused by the alloying elements which occupy places in the matrix lattice. This solid solution induce a strain field in the atomic lattice of the matrix, due to the different size of the matrix atoms and the alloying elements. This strain field inhibit dislocation movement, thus the strength of the alloy is increased. The strength increase from solid solution strengthening depends on the alloy, hence its chemical composition and the size of the alloying elements in solid solution [15, 19].

Precipitates from the aging process contribute to a strength increase from inhibited dislocation movement via shearable and non-shearable precipitates [19]. Shearable precipitates may be coherent and partially coherent, while non-shearable precipitates are incoherent. As the atomic lattice of a shearable precipitate and the matrix are misaligned, the applied stress needs to exceed a critical value high enough for a dislocation to move through the precipitate (shearing) [19]. This means dislocation movement is inhibited.

Non-shearable precipitates will inhibit dislocation movement by a mechanism called Orowan looping [19]. The dislocation will bend around the precipitate when the applied force is high enough. A dislocation shear loop is left around the precipitate when the dislocation moves past the precipitate. Each precipitate that intersects the glide plane of a gliding dislocation is a pinning point. The size and distribution of the precipitates are important, as fine and well distributed precipitates give a higher strength increase due to more more pinning points for the dislocation movements [19]. Mg and Si cause both the solid solution strengthening and the precipitation strengthening in AA6xxx, due to the mechanisms described above.

Another strengthening mechanism is strengthening by grain size reduction, described by the Hall-Petch equation [15]:

$$\sigma_{\mathrm{y}} = \sigma_0 + k_y D^{-1/2} \text{ [MPa]} \tag{2.2}$$

Where the yield strength, σ_{y}, of the material varies with average grain size, D. σ_0 and k_{y} are material constants. The yield strength increases as the average grain size decreases. Extrusion is one way to achieve this strengthening mechanism, as dispersoids formed by Cr and Mn prevent grain growth during recrystallization [17]. The increased amount of grain boundary area and increased dislocation density will inhibit the dislocation movement, hence increase the strength [15]. During thermal processing such as welding, a high heating rate and cooling rate and a brief hold-up at high temperatures will reduce the grain growth. This prevents further degradation of the material with respect to this strengthening mechanism.

2.2 Welding

Welding is a joining technique where two or more metal components are bonded by a metallurgical bond, instead of a mechanical bond, like bolting [15]. The components form one solid structure after welding. In fusion welding, a heat source, e.g. an arc or a laser, melt the components (and often with a filler material) and upon solidification they are fused together [3]. The molten material forms the weld fusion zone (or weld). The high temperature during welding will spread through the zones adjacent to the weld itself. The material in these adjacent zones can experience a microstructural change due to the temperature increase, and the zone is therefore termed the heat affected zone, HAZ [15].

The HAZ can experience alterations of the material properties. Figure 2.4 illustrates the cross section of two plates joined by a single pass buttweld, the weld is indicated along with the heat affected zone, HAZ. The orange, red and yellow area represent different regions within the HAZ.

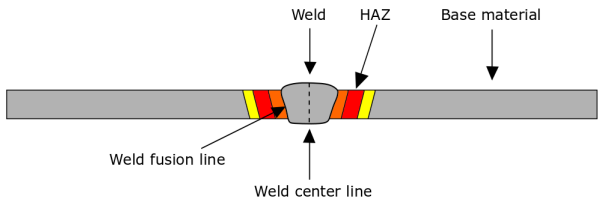

Figure 2.4: Illustration of the cross section of two sheets joined by a single pass buttweld, the weld is indicated, along with the HAZ. The orange, red and yellow area represent different regions within the HAZ.

2.2.1 Gas Metal Arc Welding

Gas metal arc welding, GMAW, also called metal inert gas welding, MIG welding, is a common welding process. It is used in a variety of industries from automotive manufacture to cross-country pipelines [3]. A wire acts as both an electrode and a filler material, and is continuously fed through a torch [3]. An arc forms between the electrode wire and the base material when current is applied to the electrode. The arc melts the wire and the base material, which form the weld pool [3]. The weld pool is protected by an inert gas shield, often argon [3]. Figure 2.5 illustrates the GMAW-process.

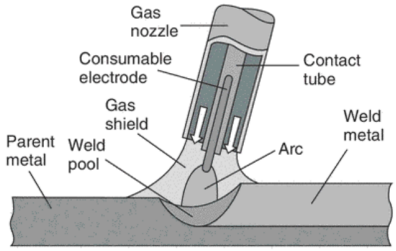

Figure 2.5: Illustration of the GMAW-process. Copied from [3].

The process is easily automated and with a continuously fed wire the welding speed can be increased. There are several advantages to automated GMAW [3]:

- Consistent quality
- Reduced defects
- Narrower HAZ due to less heat input
- Higher production rates

GMAW is a common welding process for the AA6xxx. Common filler material for welding of the AA6xxx are the AA4043 and AA5356. These alloys have higher amount of Si and Mg respectively, to reduce the risk of weld metal cracking. In the weld fusion zone the arc melts the filler and base material, resulting in an as-cast microstructure [3]. The HAZ will be further discussed in section 2.2.3.

2.2.2 Moving Heat Source Model for Welding

The heat flow problem in welding can be approximated by an analytical approach [4]. Relatively simple equations describing the temperature-time distribution during the welding are possible to derive. Heat loss from free surfaces is usually negligible in welding, as the heat loss is partially due to radiation and convection [4]. The fundamental differential equation for non-steady heat conduction in solids can be solved to obtain the temperature distribution. The differential equation for three-dimensional heat conduction [4]:

$$\frac{\partial T}{\partial t} = a\left(\frac{\partial^2 T}{\partial x^2} + \frac{\partial^2 T}{\partial y^2} + \frac{\partial^2 T}{\partial z^2}\right) \tag{2.3}$$

T is the temperature, t is the time, x, y and z describe the heat flow directions, a is the thermal diffusivity. The thermal diffusivity, a, the thermal conductivity, λ, the density, ρ, and the heat capacity, c, are related through:

$$a = \frac{\lambda}{\rho c} \tag{2.4}$$

Equation (2.3) has one and only one solution for a set of given initial and boundary conditions [4]. The analytical solution of Equation (2.3) assumes constant thermal properties

of the material. In reality, the thermal properties are dependent on temperature, as well as chemical composition and thermal history [4]. The analytical solutions therefore have limitations, but averaged values for these properties give reasonable results [4].

The Rosenthal thick plate solution is an equation describing the pseudo-steady state temperature distribution during welding with a moving point heat source with constant speed in a semi-infinite isotropic body [4]. Heat loss through radiation and convection are neglected, while conduction of heat is assumed in all three directions. Rosenthal [22] was the first to derive the relation, but the theory has later been extended and refined by others [10]. The model by Rykalin [10, 4] obtains the Rosenthal thick plate solution as:

$$T - T_0 = \frac{q_0}{2\pi\lambda}\left(\frac{1}{R}\right)\exp\left[-\frac{v}{2a}\left(R + x\right)\right] \tag{2.5}$$

Where the distance, R, from the moving point heat source is described by:

$$R = \sqrt{x^2 + y^2 + z^2} \tag{2.6}$$

T is the temperature in the point at distance R, T_0 is the start temperature, q_0 is the net heat input, λ is the thermal conductivity, a is the thermal diffusivity and v is the welding speed. The moving point heat source is applied at $x = 0, y = 0, z = 0$ in the coordinate system, with the welding speed, v, and welding direction in the x-direction.

The arc delivers a net power, q_0:

$$q_0 = \eta I U \tag{2.7}$$

Where I is the welding current and U the arc voltage. The arc efficiency factor, η, is adjusted to make a good correlation between the theoretical models and experimental data. The arc efficiency factor, η, ranges between 0.65-0.85 for GMAW [4]. The Rosenthal thick plate solution is illustrated in 3D in Figure 2.6. The welding direction is in the x-direction.

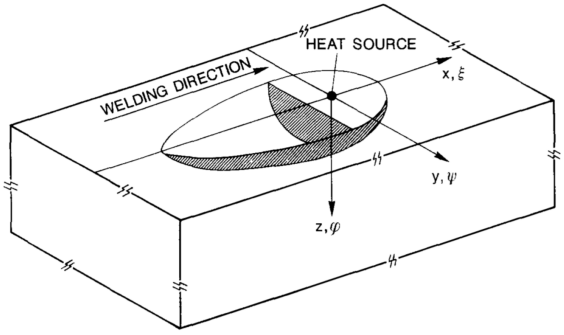

Figure 2.6: Rosenthal thick plate solution illustrated in 3D. Welding direction is in the x-direction. Copied from [23].

The Rosenthal thick plate solution describes the temperature distribution in a semi-infinite body and works reasonably well for approximation of temperature distribution during welding of thicker components of steel [4]. A thin plate solution does also exist and works better for thinner components of aluminium, as the heat source is considered to penetrate the component as a moving line source [4]. However, a more general model exist, which gives reasonable approximations for nearly all cases [4].

The Rosenthal medium thick plate solution is valid for a moving point heat source with constant speed, v [4]. It considers an isotropic, wide plate with a finite thickness, d. It is assumed that the surfaces are impermeable to heat, so mirror reflections of the heat source are accounted for to have a net heat flux of zero through each surface, $z = 0$ and $z = d$ [4]. By adding imaginary heat sources to the thick plate solution, the Rosenthal medium thick plate solution is obtained as the convergent series [4]:

$$T - T_0 = \frac{q_0}{2\pi\lambda} \exp\left(-\frac{vx}{2a}\right) \times \sum_{i=-\infty}^{i=+\infty} \left(\frac{1}{R_i}\right) \exp\left(-\frac{v}{2a} R_i\right) \tag{2.8}$$

where

$$R_i = \sqrt{x^2 + y^2 + (z - 2id)^2} \tag{2.9}$$

The Rosenthal medium thick plate solution describes the temperature, T, in the point at distance R_0, during welding. Figure 2.7 illustrates the "method of images". The real heat source $2q_0$ and the imaginary heat sources ...$2q_{-2}, 2q_{-1}, 2q_1, 2q_2$,... each located at a distance of $\pm 2id$ from the real heat source.

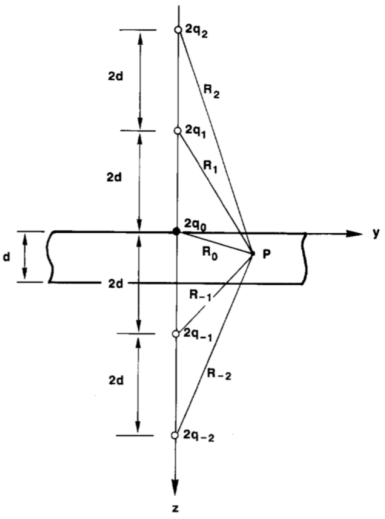

Figure 2.7: Illustration of the real and imaginary heat sources from the Rosenthal medium thick plate solution. Copied from [4].

The temperature distribution during welding is the key to understand the metallurgical changes in the HAZ from the welding procedure. The analytical solution have proven to predict the weld thermal cycles well compared to measured data [23]. Figure 2.8 illustrates the coherence of the predicted and measured weld thermal cycle in aluminium welding for fixed values of T_p, by the Rosenthal medium thick plate solution [23]. The practicality of a relatively precise and simple analytical solution compared to a complex finite element method model has a great potential.

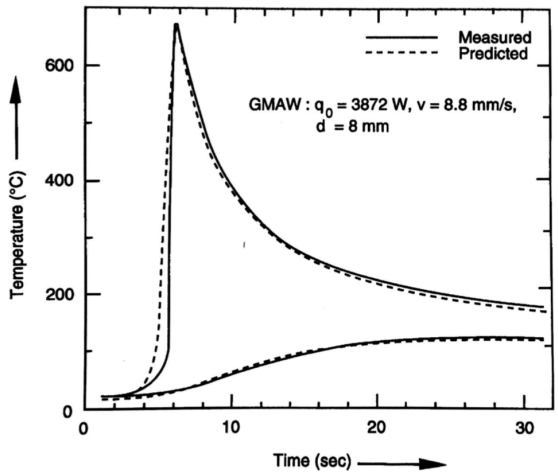

Figure 2.8: Comparison of the predicted and measured weld thermal cycle in a fixed point in the HAZ for MIG welding of aluminium, in a study by Myhr and Grong [23]. Predictions by the Rosenthal medium thick plate solution. Copied from [4].

2.2.3 The Heat Affected Zone

The AA6xxx are known to be reasonably weldable, however a significant loss of mechanical properties in the HAZ is observed [5, 4]. Precipitation is the main contributor to the good mechanical properties of AA6xxx, while coarsening of the precipitates during welding cause the degradation of the mechanical properties in the HAZ.

The HAZ is a very complex region. The material has experienced a temperature gradient with very high temperature close to the weld fusion line and a decreasing temperature throughout the adjacent area. The HAZ is commonly divided into different regions. Closest to the weld fusion zone the temperature and cooling rate were high enough to solution heat treat the base material, i.e. cause full reversion of the β''- and β'-precipitates [24, 4]. Partial melting of the grain boundaries and coarsening of some precipitates [3] can occur due to the temperature gradient in this region. However common practice accepts full reversion of precipitates. The fully reverted region, can be seen as Zone 1 in Figure 2.9 and

in Figure 2.10a. In this region, the reversion of β''- and β'-precipitates will cause a SSSS. Upon room temperature storage, clusters (and GP-zones) will form and a T4 temper will eventually be achieved. The mechanical properties can be recovered to some extent by natural aging [4], but will not reach the properties of the base material.

The partly reverted region follows next and is illustrated in Figure 2.9 as Zone 2 and in Figure 2.10a. A significant drop in mechanical properties is caused by coarsening of the precipitates and depletion of solute elements in solid solution. The mix of coarse β'-precipitates in this region with the depletion of solute elements defines the weakest point in the entire HAZ. Through the partly reverted region, the precipitates will experience less and less coarsening in addition to less depletion of solute elements, until the unaffected base material is reached. The mechanical properties in this zone increase with increasing distance from the weld center line. Figure 2.9 also illustrates how the precipitate size distribution will change before and after natural aging after welding and the respective improvement of the mechanical properties.

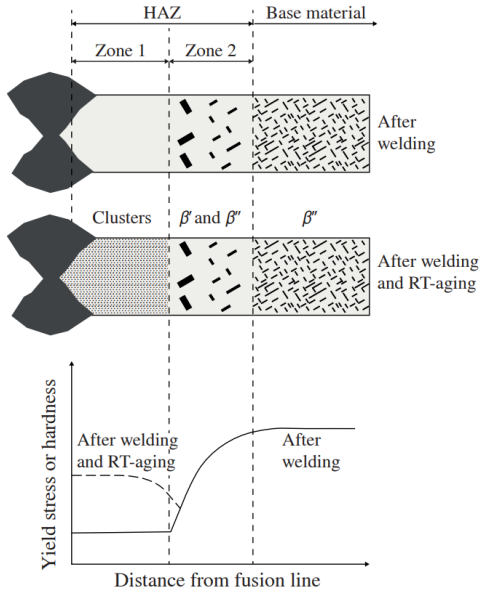

Figure 2.9: Illustration of the precipitate size distribution from welding and subsequent natural aging in the HAZ. Copied from [24].

An illustration of the hardness profile of the HAZ can be seen from Figure 2.10, which reflect how the response of natural aging from the fully reverted region in the HAZ regain some of the lost strength. The temperature for the different responses are also depicted in Figure 2.10a and 2.10b. The fully reverted region where the temperature succeeded about

500°C, partially reverted region from 250-500°C and the unaffected material where the temperature was kept below 250°C [4, 24]. The weakest point in the HAZ will after the natural aging response, appear where the temperature was about 430°C [4].

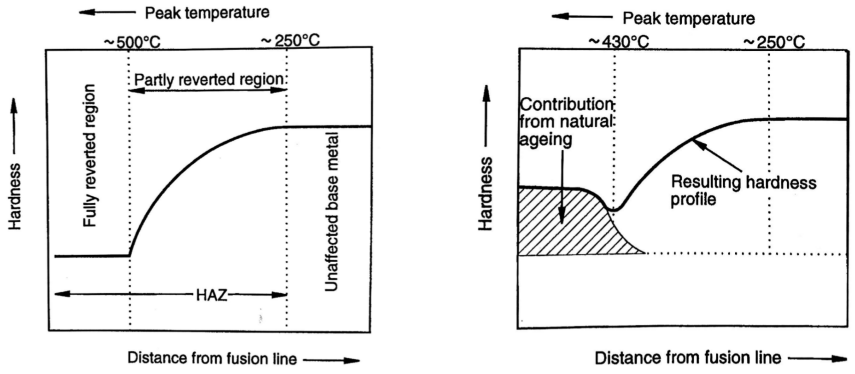

Figure 2.10: Illustration of the hardness profiles after welding of a 6082-T6 alloy **(a)** before natural aging and **(b)** after natural aging of the solution heat treated zone. Copied from [4].

2.3 Modification of the HAZ

Welded components subject to uniaxial load perpendicular to the weld will experience a stress concentration in the weakest point within the HAZ. The weakest point form a line on each side of the weld, perpendicular to the load direction. The maximum load, F, is limited by the weakest point. An invention by Furu and Myhr [25] proposes a method and an apparatus to increase the load bearing capacity by LPWHT of a welded aluminium alloy component. A welded component has initially a HAZ with reduced load bearing capacity. A heat source is applied at defined positions in the welded component, hence the areas of the HAZ along the weld are enlarged by the LPWHT. The proposed method claims to enhance the force distribution across the weld, thus providing an improvement of the load bearing capacity of the component. The general idea is illustrated in Figure 2.11, where a welded plate is subject to a uniaxial load perpendicular to the weld before and after LPWHT. The load bearing capacity is improved, i.e. $F' > F$, as a result of the modified HAZ geometry (colored red) according to the method by Furu and Myhr [25].

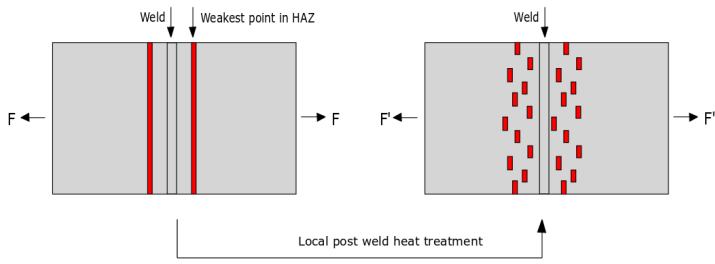

Figure 2.11: Illustration of a welded plate subject to uniaxial load perpendicular to the weld before and after local PWHT. The load bearing capacity is improved, i.e. $F' > F$, as a result of the modified HAZ geometry (colored red) according to the method by Furu and Myhr [25].

2.3.1 Local Post Weld Heat Treatment

Induction is a possible LPWHT method for HAZ geometry manipulation. Laser and cross welds have previously been tested by Hamarsnes [6] and Gjertsen [7] with both varying and promising results.

Heat treatment by induction heating is not a new technology. In fact, induction melting has been around since the early 1900's and induction heating of steels for surface hardening began in 1927 [26]. Induction is still frequently used in the metals-processing industries in applications such as preheating prior to metalworking, heat treating both of the surface and through-thickness, melting and welding [26]. Induction is commonly used in steel processing, especially for induction hardening to improve strength, wear and fatigue properties of steels [26].

Induction heat is generated by two mechanisms of energy dissipation, energy loss through Joule heating and energy loss through magnetic hysteresis [26]. In non-magnetic materials such as aluminium, copper and austenitic steels, Joule heating is the only mechanism of heat generation. It is also the primary mechanism in ferromagnetic metals, like ferritic steels. The first and primary mechanism is caused by induced Eddy-currents in the workpiece. A magnetic field is associated with both alternating and direct currents [26]. The induction coil is made of a continuous electrical conductor with turns, i.e a copper wire. When current flows through the coil a magnetic field is created around the coil. When a alternating current flows trough the coil the magnetic field changes magnitude and direction with time. The magnetic flux will vary, which induces a voltage and an Eddy current in the opposite direction to the coil current within the workpiece [26]. The electrical energy related to the voltage drop that occurs is converted to heat or thermal energy, a process called Joule heating [26].

The second mechanism, energy loss through magnetic hysteresis, applies to ferromagnetic metals. It is a less important mechanism of generating heat via induction [26]. Magnetic hysteresis losses can be simply explained as friction between magnetic dipoles as the metal is magnetized in one direction and then in the opposite direction and so on, due to the alternating current. Heat is dissipated from the energy that is required to change the direction and at rate dependent on the frequency of the alternating current [26].

Induction heat treatment is easily automated and controlled [26], hence allowing for a completely automated process with both welding and induction. Induction heating offer several other advantages such as [26]:

- Rapid heating
- Energy efficient
- High production rates
- Safe and clean working conditions
- Low maintenance requirements

2.3.2 Stationary Heat Source Model for Induction

Rykalin [10] developed a model to simulate the thermal field from an instantaneous point heat source, which have been used in a study by Østhus et al. [9]. The model can be used to simulate the thermal field from a stationary applied heat in a semi-infinite isotropic body. In the present case, the model is applied to fit an induction heat source. The model is described by the following equation [9]:

$$dT = \frac{dq}{\rho c(4\pi at)^{3/2}} \exp\left(-\frac{(x-x')^2+(y-y')^2+(z-z')^2}{4at}\right) \tag{2.10}$$

Where dT is the change in temperature in position (x, y, z), dq is the heat input, ρc is the volume heat capacity, a is the thermal diffusivity and t is the time of the applied heat from the heat source applied at position (x', y', z'). The model is illustrated in Figure 2.12, where the instantaneous stationary point heat source Q is located at (x', y', z') and the point R, located at (x, y, z) will experience a change i temperature due to the heat source, Q.

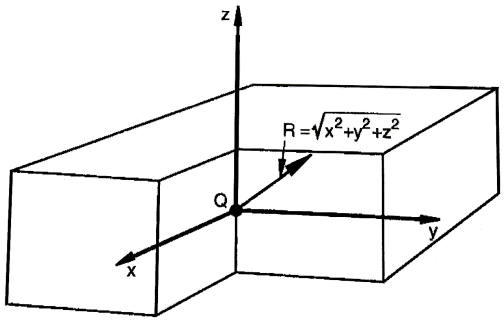

Figure 2.12: Illustration of an instantaneous stationary point heat source Q, located at (x', y', z'). The point R, located at (x, y, z) will experience a change i temperature due to the heat source. Copied from [4].

The heat input, dq, can be written as the power input, P, times the derivative of time, dt:

$$dq = Pdt \tag{2.11}$$

The induction heat source is applied at the surface of the plate, i.e. $z' = 0$. For an infinitely wide and long plate with a given thickness, d, the "method of images" is used. Figure 2.7 described in Section 2.2.2, illustrates the "method of images" or addition of imaginary heat sources. This is applied in the Rosenthal medium thick plate solution, Equation (2.8). The same principal is applied to the case of stationary heat source modelling in Equations (2.12) and (2.13) as done in the study by Østhus et al. [9]. The resulting equation is:

$$dT = \sum_{i=-\infty}^{i=+\infty} \frac{Pdt}{\rho c(4at)^{3/2}} \exp\left(-\frac{(x-x')^2+(y-y')^2+(z-2id)^2)}{4at}\right) \tag{2.12}$$

Numerical integration of Equation (2.12) was used in the study by Østhus et al. [9] to simulate induction heating. By integration of Equation (2.12) with respect to time, t, the

temperature is obtained for a point (x, y, z) as a result of an applied heat source in the point (x', y', z') after the time, t:

$$T - T_0 = \int_{t=0}^{t} \frac{P}{\rho c (4at)^{3/2}} \exp\left(-\frac{(x-x')^2 + (y-y')^2)}{4at}\right) \cdot \sum_{i=-\infty}^{i=+\infty} exp\left(-\frac{(z-2id)^2}{4at}\right) dt \tag{2.13}$$

Where T is the temperature in point (x, y, z), T_0 is the start temperature, P is the power input, ρc is the volume heat capacity, a is the thermal diffusivity and t is the time of the applied heat source at the surface with position (x', y') on a plate with thickness d.

The described analytical model, has been used to simulate an induction heat source applied on the surface of a component in the study by Østhus et al. [9] with promising results.

2.3.3 Global Strength Recovery in the HAZ

The AA6xxx experience a significant strength reduction in the HAZ after welding [4]. Østhus et al. [9] have investigated the possibility of HAZ manipulation to improve the structural properties of welded aluminium extrusions based on the invention by Furu and Myhr [25]. The objective of the study by Østhus et al. [9] was to simulate if the structural properties of welded aluminium extrusion could be improved by applying a LPWHT by a stationary heat source in the HAZ. The proposed idea will break up the straight line that forms the HAZ to create a more complex HAZ geometry. This is done by applying a local stationary heat source, e.g. by induction. The weakest point in the HAZ will not be a straight line parallel to the weld, but as a pattern decided by artificial intelligence to optimize the structural properties, i.e. the load bearing capacity. The complete simulation flow chart is illustrated in Figure 2.13. The results of Østhus et al. [9] were based on simulation of the different heat treatment steps, and are promising. A 20% improvement of the maximum load was predicted [9].

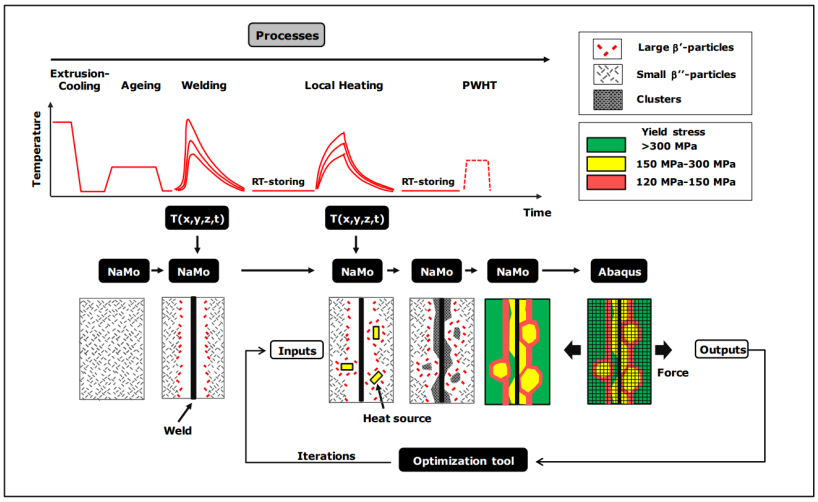

Figure 2.13: The complete simulation flow chart by Østhus et al. [9], showing the basic principles of the simulation concept of HAZ manipulation.

The preceding specialization project [8] initiated an investigation of the effect of applying a LPWHT by induction heating on the HAZ of welded 6082-T6 aluminium sheets. It was observed that a new HAZ is created around the imprint of the induction coil. Hardness testing of the area subject to LPWHT points towards a reversion of precipitates were the temperature exceeds 500°C, which will naturally age to a T4 state in ambient temperatures.

2.3.4 Post Weld Heat Treatment

A PWHT is in some cases used to minimize the degradation of the HAZ after welding. Standard PWHT is a global heat treatment similar to artificial aging. Figure 2.14 describes the precipitate size distribution after artificial aging, welding and PWHT. The extent of the HAZ is indicated by the semi-circle. The HAZ is as mentioned previously, divided into the fully reverted, the partly reverted region, and the unaffected region. The weakest point in the partly reverted region, where overaging has occured, is essentially unaffected by standard PWHT of 185°C for 5.5 hours [12]. The region is virtually depleted of solute elements, leaving the aging response very weak. The fully reverted region on the other hand will essentially regain the strength of a T6 temper during a PWHT of 185°C for 5.5 hours. The solute elements enter a SSSS state due to the high temperature and high cooling rate from the welding, and precipitate as fine β''-needles during the PWHT.

A PWHT after LPWHT is used in the simulations by Østhus et al. [9] and predicted a significant strength increase after HAZ modification. The maximum load bearing capacity is increased by up to 9.4% after HAZ modification without PWHT, while a maximum increase of 20% is observed with a PWHT.

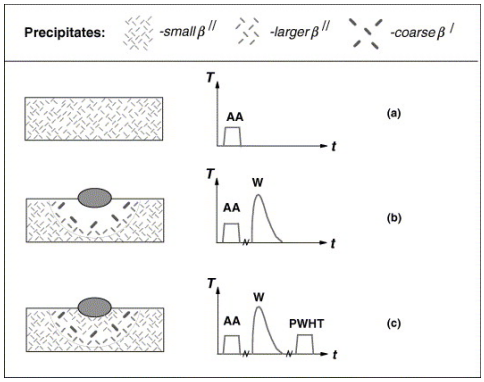

Figure 2.14: Illustration of the precipitate size distribution during multistage thermal processing of AA6xxx. Copied from [12].

2.4 Mechanical Properties of Welded Aluminium Structures

The load bearing capacity of a welded structure is the mechanical property of interest in the methodology by Furu and Myhr [25], and Østhus et al. [9]. The load bearing capacity, σ_{max}, expressed in [MPa] of a structure where the load, F, is applied by a tensile (or compressive) force, can be expressed as:

$$F = \sigma_{\text{max}} A \tag{2.14}$$

Where A is the cross section area. The load bearing capacity is the maximum stress before yielding in the component occurs. A welded component will experience a stress concentration in the weakest point in the HAZ. The strength of the weakest point in the HAZ will therefore determine the overall load bearing capacity of the structure. Additional material is utilized to compensate for the strength loss in the HAZ after welding and the weight of the overall structure will therefore increase, hence not utilizing the strength to weight ratio of the material.

Upon designing a welded component, the reduced strength in the HAZ has to be accounted for. Design codes, like Eurocode 9 [27], account for this reduction, however they are considered conservative [28]. Table 2.2 lists the characteristic values of yield strength, σ_{y}, for unwelded and HAZ of EN AW 6082-T6 plates/sheets (P/S) and extruded profiles (EP) from Eurocode 9 [27]. t is the thickness of the plates/sheets/profiles and ρ_{HAZ} is the HAZ reduction factor.

Table 2.2: Characteristic values of yield strength, σ_{y}, for unwelded and HAZ of EN AW 6082-T6 plates/sheets and extruded profiles from Eurocode 9 [27]. P/S - plates/sheets. EP - extruded profiles. t is the thickness and ρ_{HAZ} is the HAZ reduction factor

	t [mm]	σ_{y} [MPa]	$\sigma_{\text{y,HAZ}}$ [MPa]	$\rho_{\text{y,HAZ}}$
P/S	≤ 6	260	125	0.48
EP	≤ 5	250	125	0.50

For the common filler material AA5356, the strength value is σ_{w} = 210 MPa [27]. For accordance with Eurocode 9 the maximum load bearing capacity, σ_{max}, (2.14) should be calculated with respect to the HAZ value of the yield strength, $\sigma_{\text{y,HAZ}}$, i.e. $\sigma_{\text{max}} = \sigma_{\text{y,HAZ}}$. Hence a drastic decrease of the load bearing capacity, σ_{max}, is observed.

The hardness in [HV], is related to the yield strength, σ_{y} and through the relations [4]:

$$\sigma_{\text{y}} = 3.0\text{HV} - 48.1 \text{ [MPa]} \tag{2.15}$$

This equation is applicable for the hardness profile across the HAZ. Hence one can calculate the load bearing capacity before yielding from the lowest yield strength value obtained from the hardness profile of the HAZ by implementing this value into equation (2.15) for the maximum stress, σ_{max}.

2.5 The NaMo software

The NaMo software developed by O.R. Myhr et al. [11, 12, 13, 14] is a combined precipitation, yield strength and work hardening software used to estimate the precipitate size distribution and hence the strength evolution in AA6xxx during multistage thermal processing. The model has been used as a guidance tool to estimate the mechanical properties of AA6xxx by Norsk Hydro ASA for nearly two decades. It is capable of handling thermomechanical processing such as artificial aging and welding to name a few. The precipitation of MgSi-phases is the most important mechanism to describe the mechanical properties of the AA6xxx [14].

The software is based upon physical metallurgical relations, some of which were described earlier. The most recent version of NaMo, called NaMo-Version 3, utilizes Kampmann-Wagner formalism, where precipitation, growth, coarsening and dissolution is modelled as coupled processes [14]. The precipitates are assumed to be spherical, not rod or needle shaped, an assumption which can be argued to be reasonable [14]. The software calculates the precipitate size distribution as a result of an input in the form of temperature-time during thermomechanical processing.

The resulting precipitate size distribution is used in a yield strength model based around the inhibition of dislocation movement by precipitation hardening, solid solution hardening and dislocation hardening to calculate the strength contribution. A work hardening model ensures that the dislocation density is accounted for. The calculated precipitate size distribution, and hence yield strength, after thermomechanical processing is output from the software (to name a few). The software is a great tool to estimate material properties through complex thermomechanical processing of AA6xxx and has proven to give reasonable estimates.

Chapter 3

Experimental

In this chapter the experimental work from this and the preceding study [8] is described in detail.

3.1 Material and Processing

3.1.1 Base Material and Thermal Processing

The material in this project is the aluminium alloy EN AW 6082.50 and was delivered by Hydro. The chemical composition is within the Hydro specification for 6082.50, and was further analyzed with a spectrograph by SINTEF Manufacturing AS at Raufoss. The chemical composition from the spectrography is given in Table 3.1.

Table 3.1: Chemical composition of the alloying elements in the base material EN AW 6082.50. The remainder is Al.

	Alloying element [wt%]				
	Fe	Si	Cu	Mg	Cr
Measured	0.188	1.023	0.013	0.658	0.010
U(95%)	0.00222	0.01938	0.00132	0.00268	0.00027
	Mn	Zn	Zr	Ti	Ni
Measured	0.521	0.005	0.001	0.015	0.000
U(95%)	0.02121	0.00193	0.00069	0.00043	0.00277

The material followed two different homogenization routes. Homogenization parameters are listed in Table 3.2. Batch B was homogenized at a higher temperature for a shorter time compared to D, which was subject to a lower homogenization temperature for a longer holding time. The difference in homogenization routes resulted in a different recrystallization resistance for each batch, with D having the best recrystallization resistance. SINTEF Manufacturing AS carried out the homogenization.

Table 3.2: Homogenization parameters for the material EN AW 6082.50.

ID	T_{hom}[°C]	t_{hold}[h]	$t_{heating}$[h]	$t_{cooling}$[h]
B	575	2.25 (Time at temp)	4	0.5
D	535	5 (Time in furnace)	4	0.5

Extrusion was carried out at Hydal Aluminium Profiler AS at Raufoss. Extrusion parameters are listed in Table 3.3. The extrusion took place with billets with a diameter of 305 mm with a spreader plate. The extruded sheets had a width of 420 mm and 4 mm thickness.

Table 3.3: Extrusion parameters for the base material EN AW 6082.50.

T_{billet} [°C]	Ram speed [mm/s]	Puller [m/min]	Puller [kg]
485	2.3	6.5	290

Solution heat treatment and artificial aging was conducted at SINTEF Manufacturing AS after storage of the extruded sheets. The solution heat treatment temperature was 540°C with a hold time of 30 minutes, before quenching in water. The water-quenching in combination with the extremely thin and wide geometry of the sheets, caused severe warping of the sheets. Artificial aging at 185°C for 5.5 hours followed the solution heat treatment after an intermediate room temperature storage of about 26.5 hours. The long intermediate room temperature storage can be explained by the attempt to straighten the sheets which will be discussed further in the following section.

3.1.2 Preparation of the Material

The extruded EN AW 6082.50 sheets were cut into sections of approximately 1.2 m in length before solution heat treatment. The water-quenching after the solution heat treatment caused the sheets to warp severely, as seen in Figure 3.1. Due to the extensive amount of warping after quenching, the sheets were attempted straightened via four point bent in a hydraulic press to straighten two sections on each profile. The sheets after four point bending can be seen in Figure 3.2. Sections of approximately 450 mm were extracted from the straightened sheets. The lack of proper equipment to straighten the sheets called for some ingenuity, hence the four point bending, and was carried out by SINTEF Manufacturing AS.

(a) **(b)**

Figure 3.1: Extruded EN AW 6082.50 sheets **(a)** before solution heat treatment, and **(b)** after solution heat treatment and water quenching.

(a) **(b)**

Figure 3.2: Extruded EN AW 6082.50 sheets **(a)** after four point bending in a hydraulic press, and **(b)** after the straightened sections were extracted.

The weld seam from the extrusion process, which is located at the center of the sheets in the extrusion direction, was removed. The machining process is visualized in Figure 3.3. The bent sections from the EN AW 6082.50 sheets were scrapped. The weld seam were then removed, before the sheets were further milled to an approximate width of 195 mm, with a weld groove of 30° and a ”nose” of 1 mm in height as illustrated in Figure 3.4.

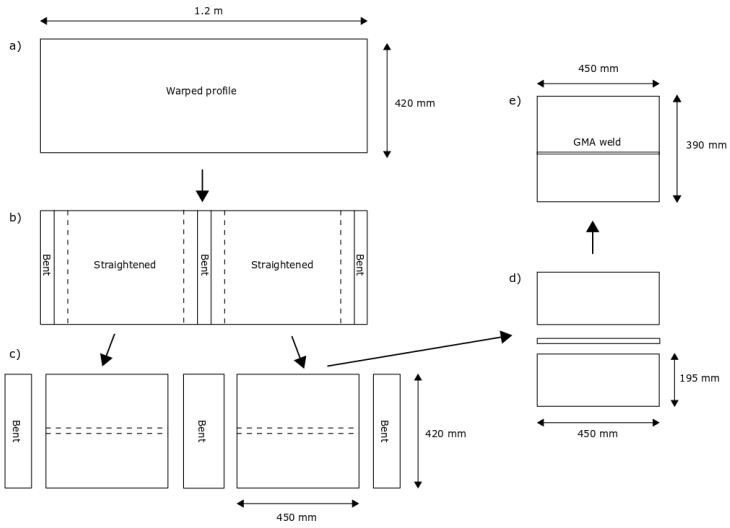

Figure 3.3: Extraction of the sections for welding. a) Warped sheet after quenching, b) straightening sections by four point bending, c) extraction of straightened sections, d) removing extrusion weld seam and milling of weld groove, e) GMAW.

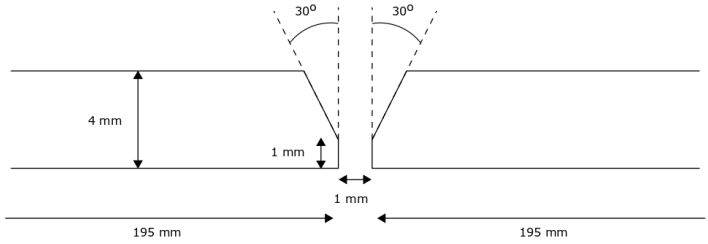

Figure 3.4: Illustration of the weld groove dimensions. Sheet width 195 mm, weld grove of 30° and a ”nose” of 1 mm.

3.1.3 Welding Procedure

The welding was carried out by a robotic GMAW procedure by Benteler Automotive AS at Raufoss together with SINTEF Manufacturing AS. Welding parameters are listed in Table 3.4. The filler wire was a 5183 aluminium alloy with composition Al4Mg5Mn, and had a diameter of 1.2 mm. Extended welding parameters are presented in the Appendix in Table D.1.

Table 3.4: Welding parameters for the robotic GMAW procedure of the 6082.50-T6 sheets.

Welding speed [mm/s]	Current [A]	Voltage [V]	Wirefeed speed [mm/s]
10	240	22	14.1

3.2 Experimental Induction Heat Input Testing

Due to laboratory access restrictions the experimental procedure of this thesis was abruptly terminated. The basis for calibration of the models in this thesis with experimental data is therefore based on the preceding study [8] that investigated the application of an induction heat treatment on the HAZ of a welded 6082-T6 aluminium alloy. The experimental procedure and some of the relevant results from the study will be briefly described here.

The induction heater, from ELVA induksjon A.S. with modelnumber R.A 16411, was supplied by SINTEF Manufacturing AS. Induction heating was carried out by clamping the induction coil onto a table and an unwelded 6082 profile was held into place on a separate table by clamping it down with steel slabs under. Thermocouples were attached on the 6082 profile in drilled holes at distances described in Table 3.5 to measure the temperature evolution in the profile. The tests were made with the induction heater set to limit current 4, the only mean of adjustment on the induction heater. The parameters for the induction were estimated from a control panel and are listed in Table 3.6. The induction coil was placed parallel, perpendicular and diagonal (45 degrees) in the length direction of the induction coil, relative to the direction of the thermocouples. The induction coil had dimensions 40 mm $\times$ 10 mm. The first thermocouple, TC1, was always placed under the center of the coil. Two runs of each placement were conducted [8].

Table 3.5: Thermocouple placement for induction heat input testing [8].

Distance from the center of induction zone [mm]				
TC1	TC2	TC3	TC4	TC5
0	4	9	16	27

Table 3.6: Induction parameters for each run during induction heat input testing [8], P1 - parallel placement of the coil run 1, N1 - normal, D1 - diagonal etc. P is the resulting power input, $P = UI$. Note that * is neglected in the averaged value.

Induction parameters							
Run	P1	P2*	N1	N2	D1	D2	Average $\pm$ SDD
$U\,[V]$	105	100*	108	NA	NA	NA	
$I\,[A]$	70	60*	72	NA	NA	NA	
$P\,[W]$	7350	6000*	7776	NA	NA	NA	7563 $\pm$ 301

The temperature evolutions during induction heating of the profile are shown in Figure 3.5. When the induction coil is parallel to the thermocouple direction, the time to reach the peak temperature of approximately 531°C is 7.5 seconds as seen in Figure 3.5a. Starting temperature was approximately 26°C. When the coil is normal to the direction of the thermocouples, the time to reach the peak temperature of approximately 480°C is 5.0 seconds as seen in Figure 3.5b. Starting temperature was approximately 33°C. The temperature evolution for both cases have a sudden increase from ambient temperature, where the heating rate is slightly decreasing to peak temperature, T_{P}. When the applied induction

is shut off at $t = t_c$, the temperature quickly drops. The temperature evolution for the rest of the runs can be seen in the appendix in Figure E.1 and E.2.

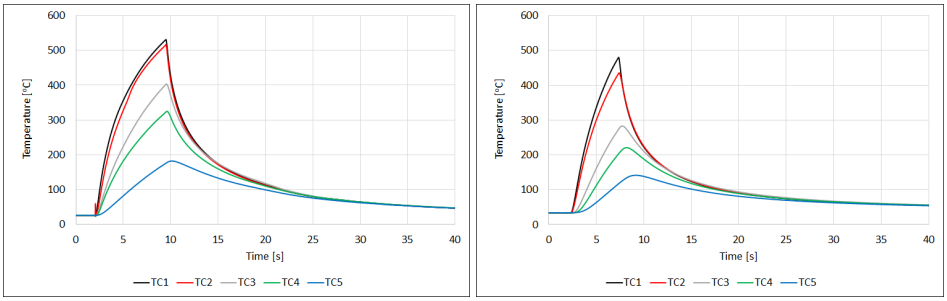

(a) **(b)**

Figure 3.5: Temperature evolution during induction heat input testing of the 6082 profile, with **(a)** the induction coil parallel to the thermocouple direction (P1), and **(b)** the coil normal to the thermocouple direction (N1).

Table 3.7 shows the peak temperatures, starting temperatures and time to reach peak temperature for the six runs. The thermocouple placement can be seen in Table 3.5. It should be noted that run P2 in Table 3.7 and Figure E.1a, where the induction coil was parallel to the thermocouple direction, reaches the peak temperature of 500.6°C at 8.6 seconds, which is significantly slower than the other the other runs. This slow time can be explained by a misplacement of the induction coil as it was observed that the center of the coil had been shifted relative to the thermocouple placement.

Table 3.7: Peak temperatures, T_P, starting temperatures, T_0, and the time to reach peak temperatures, t_c, for each thermocouple for each run during induction heat input testing.

	T_P [°C]					T_0 [°C]	t_c [s]
Run	TC1	TC2	TC3	TC4	TC5		
P1	531.2	516.7	403.5	325.1	182.3	26.2	7.5
P2*	500.6*	486.7*	382.7*	325.9*	190.4*	34.2*	8.6*
N1	480.1	435.4	283.2	220.8	141.6	33.3	5.0
N2	476.2	427.3	276.6	215.4	137.0	31.8	4.9
D1	491.3	439.5	NA	236.5	151.6	27.2	5.5
D2	506.3	450.0	302.3	256.3	159.2	28.8	5.9

3.3 Material Characterization

3.3.1 Sample Preparation

Samples were extracted from the artificially aged base material for further characterization. A Struers Labotom-5 with a 10S25 Struers cut-off wheel was used to extract the samples. Table B.1 describes the grinding and polishing steps the samples went through before hardness testing in detail. The samples were mounted in Epofix curing cold mounting resin. A Struers Tegramin-30 grinding machine was used for grinding and polishing. The samples were held in place by a sample holder and rinsed with soap water and ethanol followed by blow drying between each step. The hardness samples were plane ground with a MD-Molto 220 disk, fine ground with MD-Largo and polished with MD-Mol. This leaves the sample surface well prepared for hardness testing.

3.3.2 Hardness Testing

The artificially aged base material were subject to hardness testing. Two samples were were extracted from each batch, B 4.5 and D 6.5. The samples were hardness tested in a Zwick Roell ZHV30 hardness tester by Vickers Hardness. The impression force was set to 1 kg and dwell time 10 seconds. Indents were made with 1 mm spacing in the center line of the cross-section (2 mm beneath the surface). Ten indents were made on each sample to minimize errors.

The welded material was analyzed by SINTEF Manufacturing AS at Raufoss. Hardness indents were made in the middle of the cross section from base material hardness on one side of the weld, across the weld and to base material hardness on the other side of the weld. A hardness profile of the HAZ can be obtained from these measurements.

3.3.3 Tensile Testing

The artificially aged base material was tensile tested at SINTEF Manufacturing AS at Raufoss. Three tensile specimens were extracted from one plate from each batch, B 4.3a and D 6.4a, in both the longitudinal and transverse direction relative to the extrusion direction. The tensile specimen were strained until fracture in accordance with A.5 standard with initial cross section area of approximately 12.5 x 4 mm^2.

Chapter 4

Software Implementation and Coupling with the NaMo Software

In this chapter the implementation of the models presented in Chapter 2 is described. The NaMo software, and how the developed softwares and NaMo are coupled, is also described.

4.1 Developing the Weld Thermal Cycle Software

A Weld Thermal Cycle Software was developed based on the Rosenthal medium thick plate solution, Equation 2.8. The model was implemented in MatLab R2017b. By calculating the medium thick plate solution for each defined (x, y, z)-coordinate, a temperature distribution during welding was found. The temperature distribution was plotted in a contour-plot for graphical visualization. Material and welding input parameters are listed in Table 4.1 and 4.2 respectively. Material parameters include λ, which is the thermal conductivity, ρc, the volume heat capacity and d, the plate thickness. Welding parameters include the applied welding current, I, the arc voltage, U, the arc efficiency, η_{arc}, the starting temperature, T_0, and the welding speed, v. The thermal conductivity, λ, and the volume heat capacity, ρc, in Table 4.1, are material properties for AA6xxx currently used by Norsk Hydro ASA in many applications and by Østhus et.al [9], and is used in this thesis to get a good coherence with their models. According to Grong [4], the properties are $\lambda = 0.167\,\mathrm{W/mm^{\circ}C}$ and $\rho c = 0.0027\,\mathrm{J/mm^3{}^{\circ}C}$ for AA6xxx.

Table 4.1: Input material parameters for the Weld Thermal Cycle Software for the 6082.50-T6 sheets.

Material parameters		
λ	[W/mm °C]	0.140
ρc	[J/mm^3°C]	0.00243
d	[mm]	4

Table 4.2: Input welding parameters for the Weld Thermal Cycle Software for the 6082.50-T6 sheets.

Weld parameters		
I	[A]	240
U	[V]	22
v	[mm/s]	10
η_{arc}		0.6
T_0	[°C]	20

The thermal cycle for a point P with coordinates (x, y, z) can be obtained by solving Equation (2.8) for a fixed (y, z)-coordinate. As the welding direction is in the x-direction, the time, t can be obtained from the relation $t = x/v$, where v is the welding speed. The imaginary heat sources in a fixed point (y, z) are added until convergence, i.e. as long as the current contribution from the source of distance $\pm 2id$ is greater than 1/1000 of the last contribution from the source of distance $\pm 2(i-1)d$.

4.2 Developing the Induction Thermal Cycle Model

An Induction Thermal Cycle software was based on the stationary heat source Equation (2.10) by Rykalin. The model was also implemented in MatLab R2017b. The model is based on simple numerical integration of Equation (2.12) with respect to time for each (x, y, z)-coordinate. A temperature distribution described by (2.13) is then obtained for all points (x, y, z). The induction model is set to display both the isotherms at peak temperatures, i.e. until the induction heat source is turned off, and the thermal cycle of a specified (x, y, z)-coordinate.

Input to the model is described in Table 4.3 and 4.4. Material parameters include λ, the thermal conductivity, ρ, the volume heat capacity and d, the plate thickness. Induction parameters include the applied power, P, the efficiency of the applied power, η_{IND}, the starting temperature, T_0, and the time of applied induction, t_{c}.

Table 4.3: Input material parameters for the Induction Thermal Cycle Software for the 6082.50-T6 sheets.

Material parameters		
λ	[W/mm °C]	0.140
ρc	[J/mm^3°C]	0.00243
d	[mm]	4

Table 4.4: Input induction parameters for the Induction Thermal Cycle Software for the 6082.50-T6 sheets.

Weld parameters		
P	[W]	7563
η_{IND}		0.251
T_0	[°C]	20
t_{c}	[s]	10

Equally to the Weld Thermal Cycle software, the thermal cycle in a point (x, y, z) from a heat source applied in (x', y', z') is calculated. The imaginary heat sources are added until convergence for each step in time, i.e. as long as the current contribution from the source of distance $\pm 2id$ is greater than 1/1000 of the last contribution from the source of distance $\pm 2(i-1)d$. The change in temperature dT is then calculated for each time step.

When the time reaches $t = t_{\text{c}}$, negative heat sources are turned on. The negative heat sources are the same as described in (2.12), only negative, and simulate cooling. The total temperature is then calculated by adding the negative temperature change calculated from the negative heat sources while the temperature change from the positive heat sources continues. The temperatures will eventually converge, hence the total temperature reaches T_0.

The heat source was first distributed as a single point heat source in (x', y'). The next step was to incorporate a uniform distribution of the partial heat sources along one single line, i.e. along a line in (x', y') where y' is fixed and $x' = \pm L/2$. After the line heat sources was incorporated, a uniform distribution of heat sources applied over a section (x', y') where $x' = \pm L/2$ and $y' = \pm W/2$ was incorporated. The intensity of each partial heat source were always $P_\mathrm{i} = P/N$, i.e. the total power divided by the number of heat sources.

It was observed in a previous project that the heat was not evenly distributed over the cross section of the induction coil. The overall power from the heat source, P, can be distributed as N point heat sources over an area at the surface. If distributed with even power each partial heat source has the power, $P_\mathrm{i} = P/N$. To manipulate the distribution of the power of each partial heat source a power distribution function was made,

$$P = \sum_{i=1}^{i=N} P_\mathrm{i} = \sum_{i=1}^{i=N} \exp\left(-\left(\frac{x_i'}{k_L}\right)^2 - \left(\frac{y_i'}{k_W}\right)^2 \right) \tag{4.1}$$

Where the total power is P and the number of sources is N. k_L and k_W are variables to control the distribution of P_i. A uniform distribution of P_i is obtained when k_L or k_W approach infinity and a single point heat source is obtained when k_L or k_W approach zero. The distribution of the partial heat sources is altered by manipulating the constant k, where $k_L = kL$ and $k_W = kW$. $L = 40\,\mathrm{mm}$, $W = 10\,\mathrm{mm}$, equal to the dimensions of the cross section of the coil. The temperature in each point (x, y, z) is updated for each new partial heat source that is added at position (x', y').

4.3 Developing the Combined Weld and Induction Thermal Cycle Software

The developed Weld and Induction Thermal Cycle softwares served as a basis for a Combined Weld and Induction Thermal Cycle software where welding and LPWHT by induction is incorporated.

Figure 4.1 illustrates how the Combined Weld and Induction Thermal Cycle software is implemented. A point P in (x, y, z) is first simulated to experience a welding process. The welding thermal cycle is the same in the points (y, z) for all x, as the welding direction is parallel to the x-direction and the x-coordinate is used to calculate the time. The same point P in (x, y, z) will then experience a LPWHT by induction heating. The induction thermal cycle is calculated for a given heat source applied in the point P' with coordinates (x', y', z'). The center of the coil has to be in $x' = 0$, as the thermal cycle of welding is not described by the x-coordinate. The coils position in the y-direction controls the coils placement. $z' = 0$ as the induction heat source is applied at the surface.

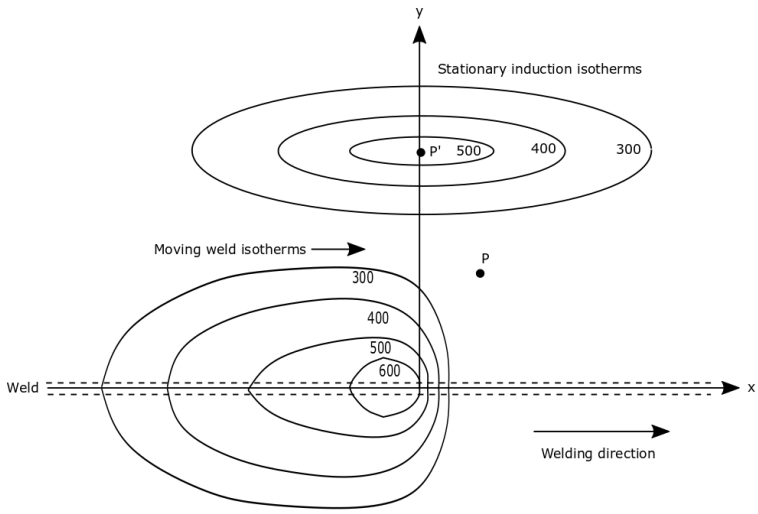

Figure 4.1: Illustration of the temperature distribution during welding and induction heat treatment.

4.4 Mechanical Properties Predicted by NaMo

The current version of NaMo can handle 12 different temperature steps. For a complex simulation like welding followed by a LPWHT like induction heat treatment, simplifications must be made. Figure 4.2 illustrates the real thermal history of a component undergoing several complex thermal processes, including:

- Quenching from SHT to RT.
- RT-storage.
- AA.
- RT-storage.
- Cooling from AA to RT.
- Welding, W.
- RT-storage.
- LPWHT.
- PWHT (or RT-storage/natural aging, NA) after LPWHT.

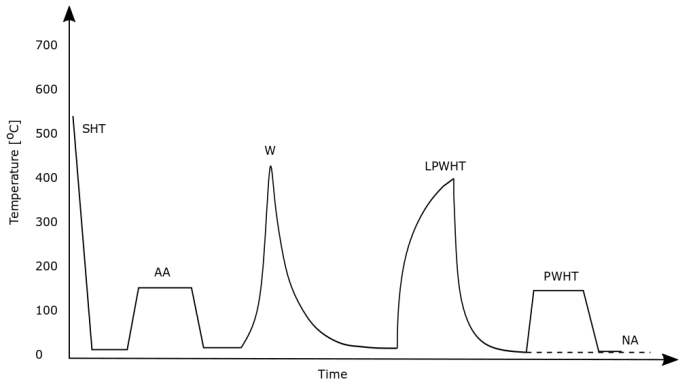

Figure 4.2: Illustration of the real thermal history. Note that the time-axis does not represent real time, and is for illustrative purposes only.

Note that the time-axis of Figure 4.2 does not represent real time, and is for illustrative purposes only. The simplified thermal history in Figure 4.3 illustrates the simplifications of the thermal processes, which include:

- T1 - T2: Quenching from SHT to RT.
- T2 - T3: RT-storage.
- T3 - T4: Heating from RT to AA.

- T4 - T5: AA.
- T5 - T6: Cooling from AA to RT.
- T6 - T7: Heating to peak temperature during W.
- T7 - T8: Cooling from peak temperature to RT after W.
- T8 - T9: RT-storage.
- T9 - T10: Heating to peak temperature during LPWHT.
- T10 - T11: Cooling from peak temperature to PWHT (or RT) after LPWHT.
- T11 - T12: PWHT (or RT-storage/NA).

Note that the time-axis of Figure 4.3 once again does not represent real time, and is for illustrative purposes only.

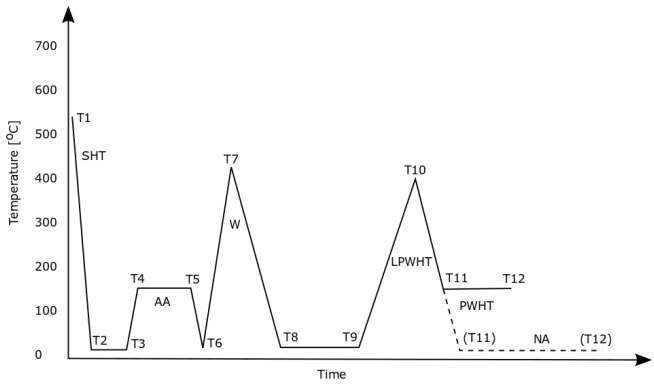

Figure 4.3: Illustration of the simplified thermal history for NaMo input. Note that the time-axis does not represent real time, and is for illustrative purposes only.

The developed Weld Thermal Cycle and Induction Thermal Cycle softwares were used to estimate the thermal cycles during welding and LPWHT by induction. The peak temperatures, time to peak and cooling time served as input in NaMo simulations. Table F.1 and F.2 in the appendix show the input for each simulation. A cooling time of 3 seconds is assumed during quenching from SHT to RT. Heating time and cooling time from AA is taken from the logging shown in Figure A.2, 2700 seconds (45 minutes) and 3600 seconds (60 minutes) respectively. RT-storage between SHT and AA was 95326 seconds (26.5 hours). The time to peak temperature during welding and induction were taken directly from the simulations. It was assumed that the cooling time could be fixed to 15s and 10s (5s) to reach 20°C (185°C for PWHT) for welding and induction respectively. RT-storage was set to 14 days and final PWHT at 185°C for 5.5 hours.

Figure 4.4 displays an example of input, the alloys composition and temperature-time, from the simplified thermal history in Figure 4.3 to NaMo. This simulation is for a specific point (x, y, z) of a 6082.50-T6 sheet undergoing SHT, RT-storage, AA, W, RT-storage, LP-WHT and RT-storage. Output data includes the resulting yield strength, which is converted to hardness by Equation (2.15). Figure F.1, F.2, F.3 in the appendix show a few more examples of input for simulations of AA, W, and LPWHT followed by a PWHT respectively, for a specific point (x, y, z) of a 6082.50-T6 sheet.

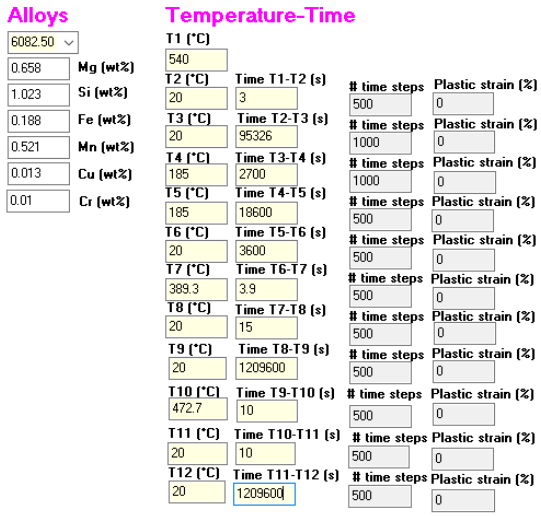

Figure 4.4: NaMo input for a welded and LPWHT 6082.50-T6 sheet.

Chapter 5

Results

The results from the mechanical analysis are first presented in this chapter. Calibration and attempted validation of the developed Combined Weld and Induction Thermal Cycle softwares are presented. Lastly, predictions of the mechanical properties by simulations in the developed Combined Weld and Induction Thermal Cycle software coupled with NaMo, are also presented.

5.1 Experimental Results

5.1.1 Mechanical Properties of the Base Material

The results from hardness and tensile testing of the 6082.50-T6 sheets SHT, AA and straightening are listed in Table 5.1.

Table 5.1: Hardness and tensile test results from the for the 6082.50-T6 sheets after solution heat treatment, aging and straightening. T - transverse and L - longitudinal direction relative to the extrusion direction.

Specimen ID	σ_y [MPa]	σ_{UTS} [MPa]	A [%]	Hardness [HV1]
B (L)	337.0 ±1.7	359.3 ±2.1	11.6 ±0.9	115.3 ±0.8
B (T)	350.7 ±1.5	364.7 ±1.5	10.8 ±0.4	
D (L)	333.0 ±1.0	355.3 ±0.6	11.1 ±0.7	113.5 ±1.0
D (T)	345.3 ±1.2	361.3 ±0.6	13.2 ±0.9	

5.1.2 Mechanical Properties After Welding

The welded 6082.50-T6 sheets were simply analyzed by SINTEF Manufacturing Raufoss AS by hardness testing of the center of the cross section across the weld. Figure 5.1a and 5.1b illustrates the measured hardness profiles of the welded 6082.50-T6 sheets for ID B.45 and ID D6.5. For B4.5 the lowest hardness value is observed at 15 mm from the weld center line, 73.9 HV and 70.5 HV. For D6.5 the lowest hardness values is observed at 13 and 15 mm from the weld center line, yielding 70.7 and 71.3 HV respectively. Base material hardness appears to be reached at about 30 mm from the weld center line, however indents should have been made until a stable hardness value was observed.

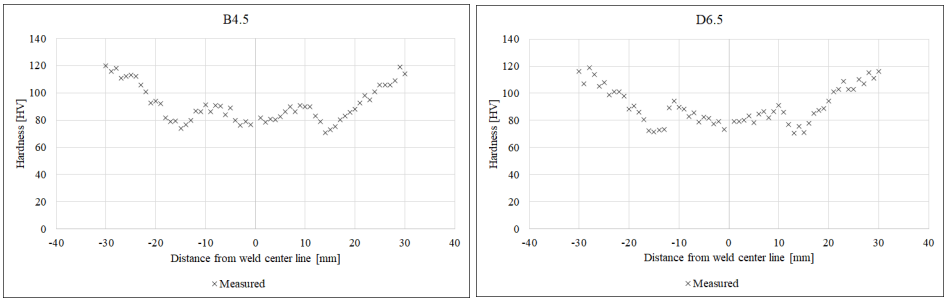

(a) **(b)**

Figure 5.1: Hardness profile of the welded 6082.50-T6 sheets, **(a)** ID B4.5 and **(b)** D6.5.

5.2 Simulation Results

5.2.1 Calibration of the Weld Thermal Cycle Software

The developed Weld Thermal Cycle software was used to estimate initial welding parameters for the 6082.50-T6 sheets. The objective was to create a wide HAZ to study the effect of the LPWHT by induction in the HAZ. For this simulation a set of welding parameters was proposed, the welding speed, v, the welding current, I, the voltage, U and the efficiency factor η_{arc}. Material parameters are presented in Table 5.2, note that the thermal conductivity, λ, and the specific volume heat capacity, ρc, differ from the rest of the simulations presented in this thesis.

Table 5.2: Input material parameters for the Weld Thermal Cycle Software during initial estimates of welding parameters for the 6082.50-T6 sheets.

Material parameters		
λ	[W/mm °C]	0.167
ρc	[J/mm^3°C]	0.0027
d	[mm]	4
T_0	[°C]	20

v was proposed to 10 mm/s, I = 200 A, U = 25 V and $\eta_{\text{arc}} = 0.8$. This predicted the 400°C isotherm to about 22 mm from the weld center line and the 500°C isotherm to about 17 mm from the weld center line. The weakest point should then be around 19-20 mm from the weld center line. Figure 5.2 displays the predicted isotherms.

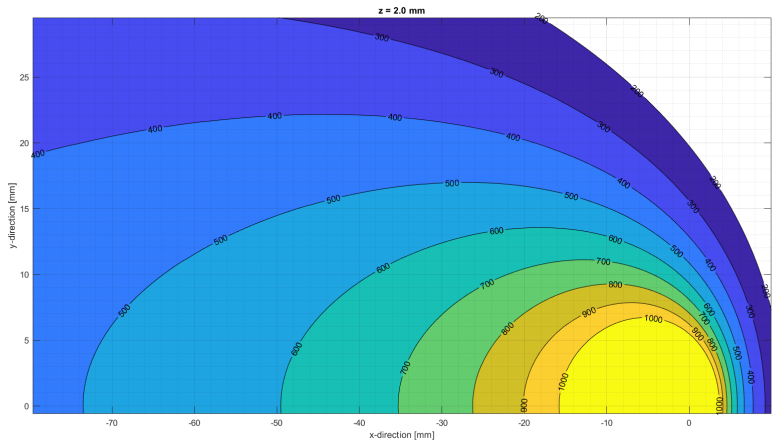

Figure 5.2: Predicted isotherms for estimates of the initial welding parameters before welding. v = 10 mm/s, I = 200 A, U = 25 V, $\eta_{\text{arc}} = 0.8$, λ = 0.167 W/mm °C and ρc = 0.0027 J/mm^3°C.

The arc efficiency factor, η_{arc}, was estimated by trial and error to fit the experimental hardness profile of the HAZ in Figure 5.1. As no thermocouples were attached to log the temperature evolution during welding, $\eta_{\text{arc}} = 0.60$ seemed to be an adequate estimate and was used for further simulations in NaMo. The η_{arc} ranges between 0.65-0.85 for GMAW according to Grong [4]. The applied welding current and arc voltage in this study were higher than normal to create a wide HAZ, along with a slow welding speed. Note that the thermal conductivity, λ = 0.140 W/mm °C, and the specific volume heat capacity, $\rho c = 0.002\,43\,\mathrm{J/mm^3{}^\circ C}$ in these simulations differ from the initial predictions. The welding operator at Benteler Automotive AS suggested v = 10 mm/s, I = 240 A, U = 22 V, which were used to weld the 6082.50-T6 sheets. Figure 5.3 displays the predicted isotherms for the welding process with these parameters.

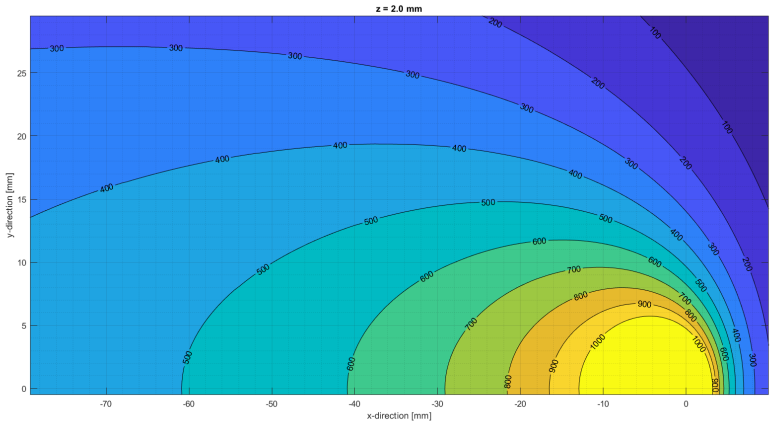

Figure 5.3: Predicted isotherms for determination of the initial welding parameters after welding. v = 10 mm/s, I = 240 A, U = 22 V, $\eta_{\text{arc}} = 0.60$, λ = 0.140 W/mm °C and ρc = 0.00243 J/mm$^3{}^\circ C$.

5.2.2 Validation of the Weld Thermal Cycle Software

The developed Weld Thermal Cycle software was attempted validated by comparison with a proven Weld Thermal Cycle Program developed by O.R. Myhr[1]. Figure 5.4a displays the output of the developed software and 5.4b shows the user interface with both input and output developed by O.R. Myhr[1] which was copied from the study by A. Hamarsnes [6]. The predicted peak temperature of the developed software is 215.5°C, while the program by O.R. Myhr predicts 215°C. The predicted time to peak temperatures is 0.1 s and 0 s respectively. The developed Weld Thermal Cycle software matches the program by O.R. Myhr well.

[1]Norsk Hydro, Raufoss

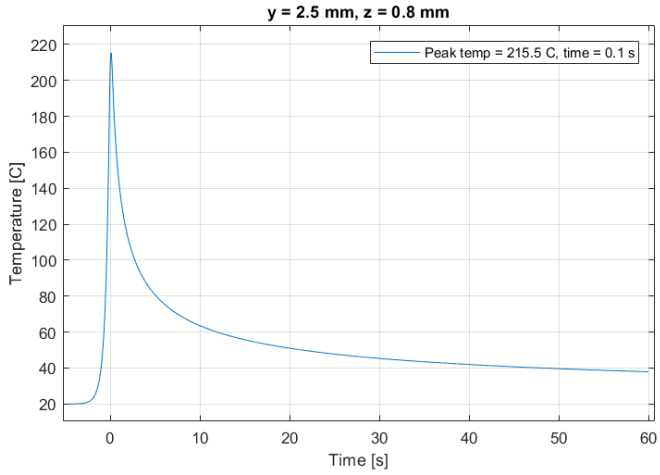

(a)

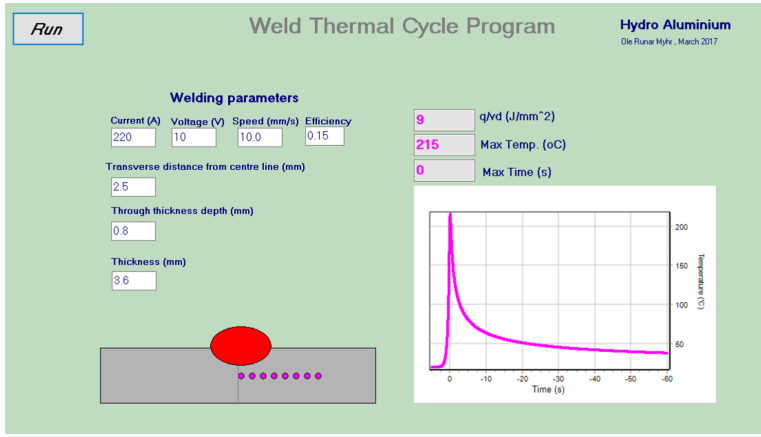

(b)

Figure 5.4: Comparison of predicted weld thermal cycles by **(a)** the developed Weld Thermal Cycle software and **(b)** the Weld Thermal Cycle Program developed by O.R. Myhr copied from [6].

5.2.3 Calibration of the Induction Thermal Cycle Software

To calibrate the developed Induction Thermal Cycle software, a set of experimental data from a the preceding study [8] presented in section 3.2 was used. The thermal measurements and their respective positions are presented in Table 3.7 and 3.5 respectively. The induction parameters are presented in Table 3.6. It should be noted that uncertainty of the data is relatively high, but should give a somewhat reasonable estimate.

By fitting the thermal measurements to the software by trial and error, the net input power from the induction coil into the 6082 aluminium profile, P_{net} was found to approximately 1900 W. The averaged output power from the induction coil, $P = 7563$ W and an efficiency factor of $\eta_{\text{ind}} = 0.251$, leaves $P_{\text{net}} = 1898$ W. P_{i} is distributed according to Equation (4.1) with $k = 0.40$ and is displayed in Figure 5.5.

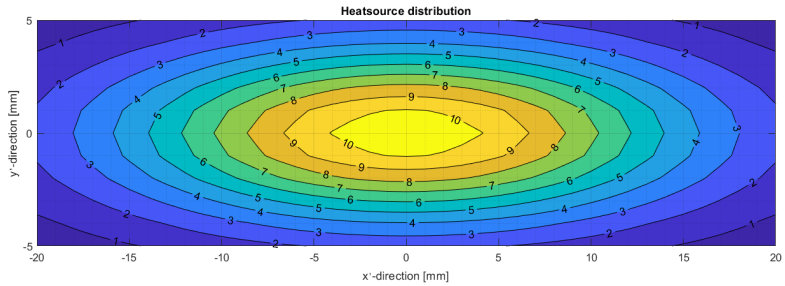

Figure 5.5: Distribution of partial heat sources, P_{i} with $k = 0.40$, $P = 7563$W and $\eta_{\text{ind}} = 0.251$, according to Equation (4.1).

Figure 5.6a displays a comparison of the experimental (measured) and simulated (predicted) thermal cycles during induction for run P1 during induction heating. Three placements of the thermocouples are presented, TC1 in the center of the coil, TC3 and TC4, respectively 9 and 16 mm away from the center of the coil in the x-direction. The start temperature, T_0, was 26.2 °C and induction was applied for $t_{\text{c}} = 7.5$ s, with $P_{\text{net}} = 1898$ W. For TC1 the measured peak temperature is 531.2 °C and the simulated peak temperature is 531.9 °C, TC3 measured 403.5 °C and predicted 450.8 °C, and TC4 measured 325.1 °C and predicted 322.6 °C.

A comparison of the experimental (measured) and simulated (predicted) thermal cycles during induction for run N2 during induction heating can be seen in Figure 5.6b. Three placements of the thermocouples are presented, TC1 in the center of the coil, TC3 and TC4, respectively 9 and 16 mm away from the center of the coil in the y-direction. The start temperature, T_0, was 31.8 °C and induction was applied for $t_{\text{c}} = 4.9$ s, with $P_{\text{net}} = 1898$ W. For TC1 the measured peak temperature is 476.2°C and the simulated peak temperature is 478.8°C, TC3 measured 276.6°C and predicted 277.2 °C, and TC4 measured 215.4 °C and predicted 180.5 °C.

Lastly the thermal cycles during induction for run D2 during induction heating is presented

in Figure 5.6c. Three placements of the thermocouples are presented, TC1 in the center of the coil, TC3 and TC4, respectively 9 and 16 mm away from the center of the coil in the xy-direction, i.e. diagonally. The start temperature, T_0, was 28.8 °C and induction was applied for $t_c = 5.8$ s, with $P_{net} = 1898$ W. For TC1 the measured peak temperature is 506.3 °C and the simulated peak temperature is 499.9 °C, TC3 measured 302.3 °C and predicted 328.7 °C, and TC4 measured 256.3 °C and predicted 217.1 °C.

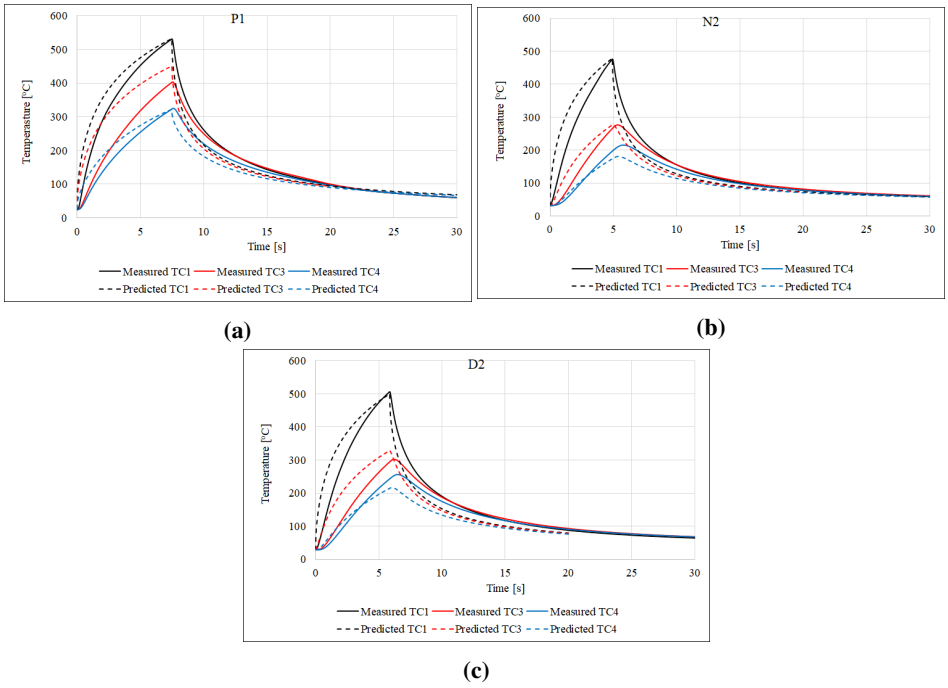

Figure 5.6: Comparison of experimental (measured) and simulated (predicted) thermal cycles during induction heating for **(a)** run P1, **(b)** run N2 and **(c)** run D2.

The measured peak temperatures were also plotted in a contour plot for calibration. This allowed all of the measured peak temperatures for each run (P1, P2, N1, ...) to be compared to the temperature represented by the predicted isotherms. Figure 5.7 shows a comparison of experimental (measured) values displayed as diamond shaped points and simulated (predicted) values displayed as contour lines of peak temperatures for run P1 and run D2, at $t = t_c$, during induction heating, described above.

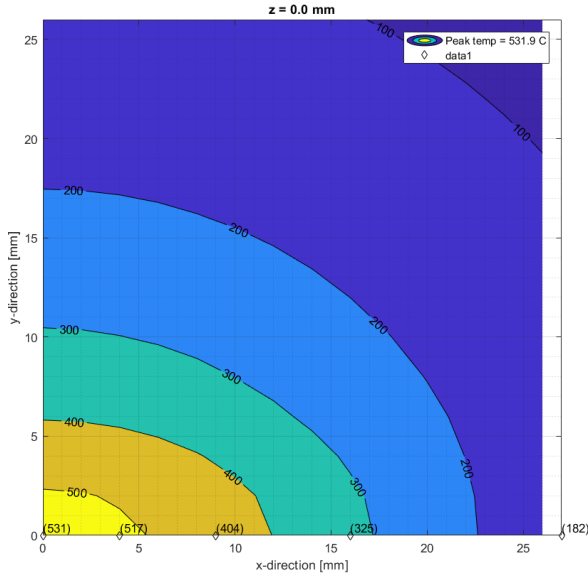

(a)

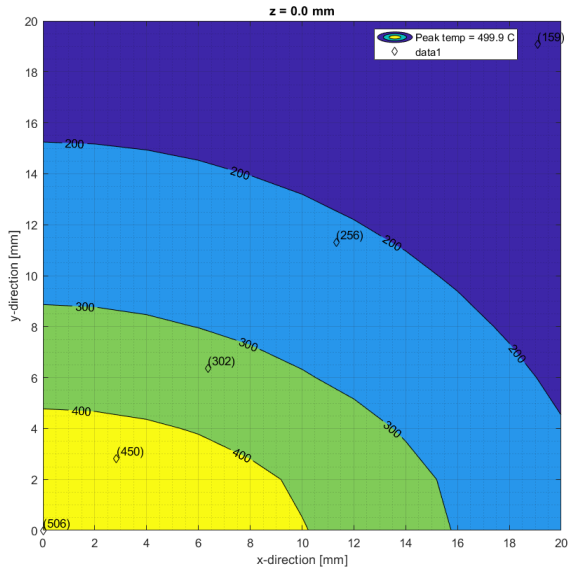

(b)

Figure 5.7: Comparison of experimental (measured) values displayed as diamond shaped points and simulated (predicted) values displayed as contour lines of peak temperatures, at $t = t_c$, during induction heating, for **(a)** run P1 and **(b)** run D2.

5.2.4 Validation of the Induction Thermal Cycle Software

The developed Induction Thermal Cycle software was attempted validated by simulating two different heat source sources, one with partial heat sources and one with a single point heat source. The time sensitivity of the software is also tested by simulating the same heat source with two different time steps.

Heat source sensitivity
Figure 5.8a and 5.8b compares predicted peak temperatures for a distribution of partial heat sources and one single point heat source respectively, with applied induction of $P_{\text{net}} = 1898$ W with $\eta_{\text{IND}} = 0.251$ at $t_{\text{c}} = 7.5$ s. The predicted peak temperatures close to the center of the induction coil $(x = y = 0)$ deviate quite significantly, which is expected. The difference in predicted peak temperatures decreases with increasing distance from the induction coil. The same applied power of induction gives a similar temperature far away from the heat source. This indicates that the discrete distribution of partial heat sources is fairly valid.

Time sensitivity
Figure 5.9a and 5.9b compares predicted peak temperatures for distribution of partial heat sources with dt = 0.1 s and dt = 0.001 s respectively. Induction applied with $P_{\text{net}} = 1898$ W for $t_{\text{c}} = 7.5$ s. The predicted peak temperature close to the center of the induction coil $(x = y = 0)$ is less than the predicted peak temperature with dt = 0.001 s. With increasing distance from the induction coil center, the difference in predicted peak temperatures decrease. A sufficient dt is required for a good simulation.

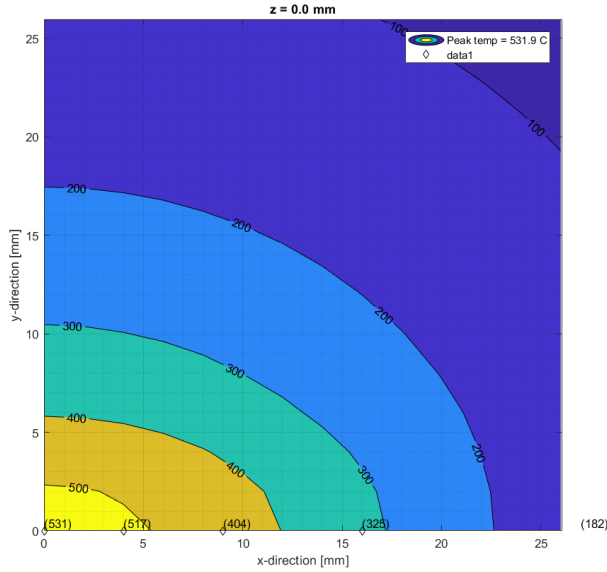

(a)

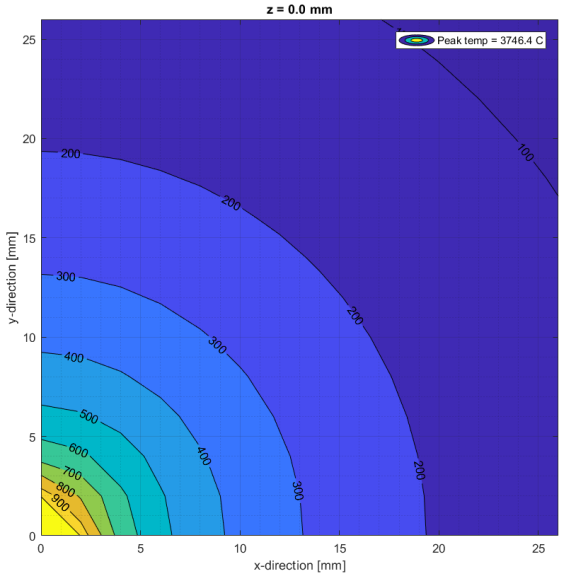

(b)

Figure 5.8: Comparison of predicted peak temperatures for **(a)** distribution of partial heat sources and **(b)** one single point heat source. Applied induction of $P_{\text{net}} = 1898$ W at $t_{\text{c}} = 7.49$.

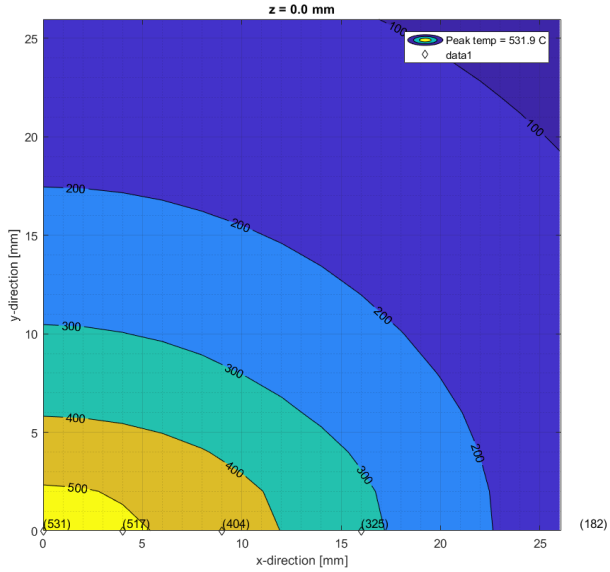

(a)

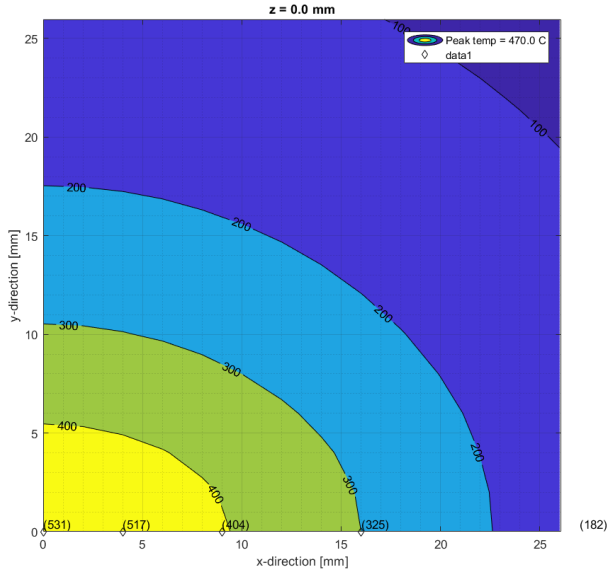

(b)

Figure 5.9: Comparison of predicted peak temperatures for a distribution of partial heat sources with applied induction of $P_{\text{net}} = 1898$ W at $t_{\text{c}} = 7.5$ s for **(a)** $dt = 0.001$ s and **(b)** $dt = 0.1$ s.

5.3 Predictions by the Weld and Induction Thermal Cycle Software coupled with NaMo

5.3.1 Predicted Hardness Profile After Welding

Simulations of the welding process was carried out using the developed Weld and Induction Thermal Cycle software. The input parameters for the welding simulations are listed in Table 4.1 and 4.2. Simulations were done to create a temperature-time profile a specific (x, y, z)-coordinate of the cross section. The temperature-time history for the (x, y, z)-coordinate from the welding simulations served as input to NaMo to estimate the mechanical properties. By repeating this process for each (x, y, z)-coordinate, a predicted hardness profile of the cross section after welding was created. The welding was simulated with the arc in $(x, y, z) = (0, 0, 0)$. The z-coordinate of the observed point was fixed to $z = 2$, i.e. the center of the thickness of the sheet, during welding. The input temperatures, times and positions are listed in Table F.1 and F.2.

The hardness profile predicted by NaMo is the exact same for B4.5 and D6.5, as the thermal processing route in NaMo does not incorporate the homogenization the 6082.50-T6 sheets were subject to before SHT and AA at SINTEF Manufacturing AS at Raufoss. Figure 5.10a and 5.10b illustrates the measured hardness profiles of the welded 6082.50-T6 sheets for ID B.45 and ID D6.5 and the predicted hardness profile from NaMo-simulations. For B4.5 the lowest measured hardness value is observed at 15 mm from the weld center line, 73.9 HV and 70.5 HV. For D6.5 the lowest measured hardness values is observed at 13 and 15 mm from the weld center line, yielding 70.7 and 71.3 HV respectively. Base material hardness appears to be reached at about 30 mm from the weld center line, however indents should have been made until a stable hardness value was observed. The predictions by NaMo estimates the lowest hardness value at 58.3 HV, 16 mm from the weld center line and base material hardness reached at 132.8 HV, 32 mm from the weld center line.

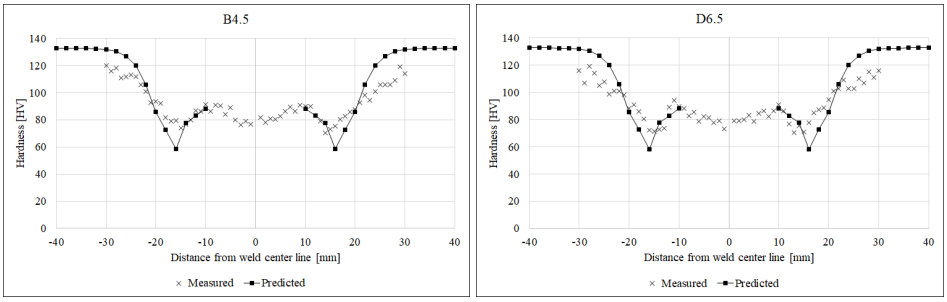

(a) **(b)**

Figure 5.10: Hardness profile of the welded 6082.50-T6 sheets, ID **(a)** B4.5 and **(b)** D6.5, and the predicted hardness profile by NaMo-simulations.

5.3.2 Predicted Hardness Profiles After Welding and LPWHT

Simulations of the welding and the subsequent LPWHT process was carried out using the developed Combined Weld and Induction Thermal Cycle software. The input parameters for the welding simulations are listed in Table 4.1 and 4.2 and the input parameters for LPWHT simulations are listed in Table 4.3 and 4.4. The addition of LPWHT adds a temperature-time profile for a specific (x, y, z)-coordinate of the cross section. The temperature-time history for the (x, y, z)-coordinate from the welding and the LPWHT simulations served as input to NaMo to estimate the mechanical properties. A predicted hardness profile of the cross section after welding and LPWHT, and with an additional PWHT was created by repeating this process for each coordinate of the cross section. Predicted hardness profiles were made for both the middle of the cross section, i.e. $z = 2$, and the surface, i.e. $z = 0$. The input temperatures, times and positions are listed in Table F.1 and F.2. The welding was simulated with the arc in $(x, y, z) = (0, 0, 0)$. The induction coil was simulated with center in $(x', y', z') = (0, 20, 0)$ with the length direction, L, parallel to the x-direction. The x-coordinate of observed point was fixed to $x = 0$ during the simulations, which is across the middle of the induction coil over the width, W.

Figure 5.11a illustrates the predicted hardness profiles of the welded 6082.50-T6 sheets before and after LPWHT by NaMo-simulations at $z = 2$. After LPWHT, the lowest hardness value is 57.6 HV at 16 mm from the weld center line, and base material hardness reached at 132.8 HV, 34 mm from the weld center line. A deterioration of the hardness of the HAZ is observed in this area.

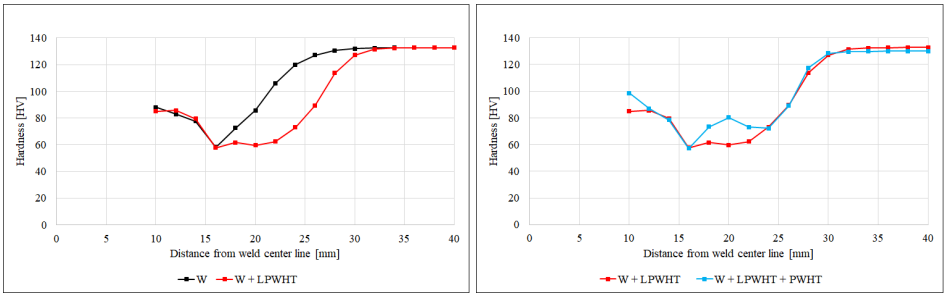

(a) **(b)**

Figure 5.11: Predicted hardness profile ($z = 2$) of the welded and LPWHT 6082.50-T6 sheets **(a)** before and **(b)** after PWHT and by NaMo-simulations. RT-storage of 14 days between welding and LPWHT, and PWHT of 185°C for 5.5 hours is simulated.

A final PWHT of 185°C for 5.5 hours was also simulated after the LPWHT to investigate the aging response of the material after LPWHT. Figure 5.11b illustrates the predicted hardness profiles of the welded and LPWHT 6082.50-T6 sheets before and after the final PWHT by NaMo-simulations at $z = 2$. The predictions by NaMo estimates the lowest hardness value at 57.2 HV, 16 mm from the weld center line, and base material hardness reached at 130.0 HV, 30 mm from the weld center line. Some strength recovery is ob-

served around 20 mm from the weld center line, reaching 80.2 HV, and approximately at the weld fusion line of 10 mm with 98.5 HV.

Figure 5.12a and 5.12b illustrates the same as Figure 5.11a and 5.11b, but at the surface of the sheet, i.e. $z = 0$. The predictions by NaMo estimates the lowest hardness value at 57.5 HV, 18 and 22 mm from the weld center line and base material hardness reached at 132.8 HV, 32 mm from the weld center line after LPWHT. After LPWHT and PWHT, the lowest predicted hardness value is 76.6 HV at 24 mm from the weld center line, and base material hardness reached at 130.0 HV, 30 mm from the weld center line. A significant strength recovery is observed between 14 and 26 mm from the weld center line, reaching 118.9 HV at max, and approximately at the weld fusion line of 10 mm with 98.5 HV.

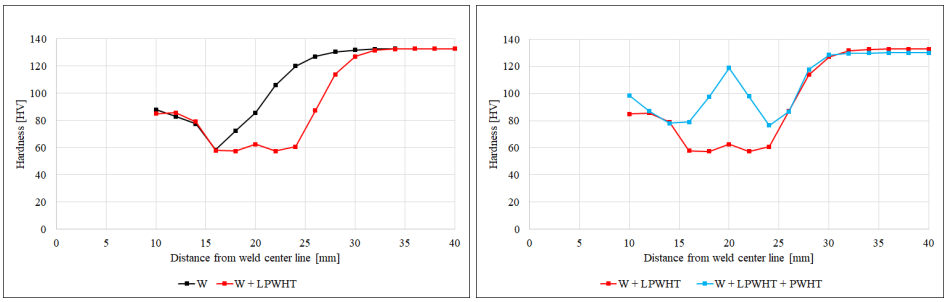

(a) **(b)**

Figure 5.12: Predicted hardness profile ($z = 0$) of the welded and LPWHT 6082.50-T6 sheets **(a)** before and **(b)** after PWHT and by NaMo-simulations. RT-storage of 14 days between welding and LPWHT, and PWHT of 185°C for 5.5 hours is simulated.

Chapter 6

Discussion

In this chapter, relevant results and findings are discussed, both experimental and predictions. The developed softwares are also discussed.

6.1 Accuracy of the Hardness Conversion

By converting the measured yield strength of the base material in Table 5.1 according to Equation (2.15), a base material hardness of 128.4, 132.9, 127.0 and 131.1 HV is obtained. The converted hardness deviates from the measured hardness by between 13.1 and 17.6 HV. The converted hardness from the measured yield strength is closer to the base material hardness predicted by NaMo of 132.8 HV. This should be kept in mind when comparing the measured and predicted hardness profiles of the HAZ. Table 6.1 shows the measured yields strength (σ_y), measured hardness and converted hardness for batch B and D both in the transverse - T and longitudinal - L direction relative to the extrusion direction. It should be noted that the relation in Equation (2.15) fits perfectly between the predicted yield strength and hardness from the simulations in NaMo.

Table 6.1: Hardness and tensile test results for the 6082.50-T6 sheets after solution heat treatment, aging and straightening. T - transverse direction and L - longitudinal direction relative to the extrusion direction, and the converted hardness from the yield strength.

Specimen ID	Measured σ_y [MPa]	Measured [HV1]	Converted [HV]
B (L)	337.0 $\pm$1.7	115.3 $\pm$0.8	128.4
B (T)	350.7 $\pm$1.5		132.9
D (L)	333.0 $\pm$1.0	113.5 $\pm$1.0	127.0
D (T)	345.3 $\pm$1.2		131.1

6.2 Developed Softwares

6.2.1 The Weld Thermal Cycle Software

The Weld Thermal Cycle Software code can be seen in Appendix G. The NaMo simulations which predict the hardness profile of the HAZ, can to some extent be used to validate the developed Weld Thermal Cycle software. The absolute difference in hardness between the averaged measured hardness profile of the HAZ and the predicted hardness profile by simulations in the developed Weld Thermal Cycle software and NaMo is shown in Figure 6.1. The hardness profiles are shown in Figure 5.10a and 5.10b in section 5.4.1. The weakest measured point in the HAZ of B4.5 and D6.5 is 70.5 HV, while the predicted weakest point is 58.3 HV.

The measured hardness profiles seem to have stabilized at 30 mm from the weld center line, as the values, 114-120 HV, are about the same as the measured hardness of the base material of 115.3 and 113.5 HV for B4.5 and D6.5 respectively. It should be noted that the base material hardness is measured with a different hardness tester and on another 6082.50-T6 sheet from the same batch which can cause some deviation. In addition the converted hardness from the yield strength differ from the measured hardness. The assumption of 15 seconds cooling to RT from the peak temperature during welding is also worth mentioning. The predicted mechanical properties could be better estimated if NaMo did not require a simplified thermal history. However the assumptions and simplifications are acceptable and give reasonable results.

The overall fit of the predicted hardness compared to the measured values is acceptable. The trend is relatively similar, even though the predictions miss by as much as 19.5 HV. A similar trend is very important as fine-tuning is required to get a better match. Thermal measurements during welding would be a nice addition, as the arc efficiency factor would be estimated better. The arc efficiency factor $\eta_{\text{arc}} = 0.6$ seems however to be a reasonable estimate, as the predicted hardness profile of the HAZ is fairly similar to the measured.

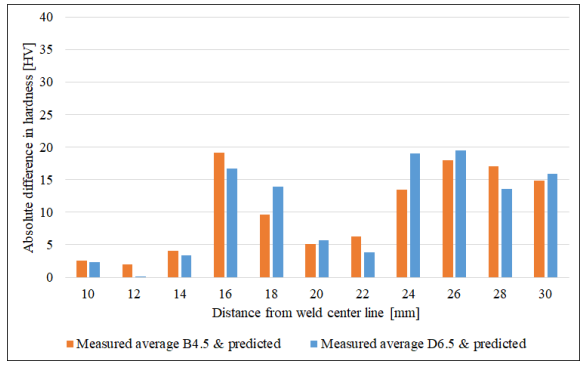

Figure 6.1: Absolute difference in hardness between the averaged measured hardness profile of the HAZ and the predicted hardness profile by simulations in the developed Weld Thermal Cycle software and NaMo.

6.2.2 The Induction Thermal Cycle Software

The Induction Thermal Cycle Software code can be seen in Appendix G. The experimental data for calibration of the Induction Thermal Cycle software should be interpreted with attention to the uncertainty it might involve. The thermocouples were drilled all the way through the aluminium sheet, leaving the top of the thermocouples exposed to direct induction. As the thermocouples are made of a different material, the real temperature of the aluminium sheet during induction heating might deviate from the temperature measured by the thermocouples.

The induction machine had an analog display of current and voltage which needed to be observed to log the values. The current and voltage was unfortunately only logged on three of the six runs (P1, P2 and N1), and run P2 is believed to be compromised, leaving current and voltage only logged for two runs. The averaged value of the output power, P =7563W, is merely a qualified guess, but is believed to be reasonable. With the discrete partial heat source distribution described by Equation (4.1), with L =40 mm, W =10 mm and $k = 0.40$, the net power input to the 6082 profile was approximated to P_{net} = 1898 W, and the efficiency factor of the induction heating to η_{IND} = 0.251. As the output power was approximated by only two runs, the uncertainty of the net power and efficiency factor for induction heating is high as well. The net power does however estimate a fairly similar thermal cycle for each thermocouple presented in Figure 5.6 in section 5.2.3.

The stationary heat source model with partial heat sources (2.13) and (4.1) might need further adjustment and calibration for induction heating. The simulated temperature on the surface in the center of the coil is higher than the temperature in the center of the sheet. Further from the induction coil the temperature is more or less equal at the surface, center and back of the sheet.

6.2.3 Combined Weld and Induction Thermal Cycle Software

The Combined Weld and Induction Thermal Cycle Software code can be seen in Appendix G. The developed Weld and Induction Thermal Cycle softwares were implemented into a Combined Weld and Induction Thermal Cycle software. The two different softwares has been described in detail, and the presented implementation, results and discussion of the two softwares should be sufficient to describe the Combined Weld and Induction Thermal Cycle software.

6.3 Weld and Induction Thermal Cycle Software Coupled with NaMo

The assumption of 15 and 10 seconds cooling time to RT after peak temperature is reached during welding and LPWHT by induction seem to give reasonable estimates of the predicted hardness by NaMo. As NaMo only takes a simplified temperature-time input this is necessary. The cooling rate after both welding and induction is very high right after the heat source is turned off and decreases as the temperature is reaching RT. The precipitates in the 6082.50-T6 are fairly stable at temperatures lower than 250 °C for shorter times, hence the increased temperature during welding and LPWHT by induction is most important close to the peak temperature.

The cooling time of 5 seconds down to PWHT-temperature of 185 °C followed by the direct PWHT, shown in section 4.4 in Figure 4.3, is more questionable. This is done due to limited temperature-time input in NaMo and the previous thermal processes are more important to estimate correctly. Even though this assumption may be rough, a precipitation response from the material because of the LPWHT and PWHT may be more noticeable. This precipitation response is very important, as it indicates that a sufficient strength recovery could be possible.

Note that simulations in this thesis is only valid for the one strip of the cross section of the HAZ that was subject to simulations. The imprint by the LPWHT varies with the x-direction and in this thesis only one x-value was simulated, $x = 0$. $x = 0$ should also experience the highest temperature increase from the LPWHT, as it is in the center of the coil. Another cross section with a different x, might only experience a degradation of the properties of the HAZ. The total load bearing capacity of a welded plate with one single imprint of the induction requires several simulations like the one presented in this thesis (for several x-values), along with a finite element simulation of the load bearing capacity. But the predicted hardness increase in the one strip of the cross section, indicates that the manipulation of the HAZ geometry suggested by Furu and Myhr [25] and Østhus et al. [9] could increase the global load bearing capacity, as it would break up the straight line formed by the weakest point in the HAZ.

6.3.1 Predicted Hardness Profiles

Figure 5.11a and 5.11b displays the predicted hardness profile after simulations with $z = 2$ and $z = 0$ respectively, of the welded and LPWHT 6082.50-T6 sheets before and after PWHT. RT-storage of 14 days between welding and LPWHT, and PWHT of 185 °C for 5.5 hours is simulated. The simulations with $z = 0$ and $z = 2$ are quite similar for natural aging of 14 days after LPWHT, however the deterioration of the HAZ is worse for $z = 0$ than $z = 2$.

The simulation with PWHT is another story. The predicted weakest point of the surface with $z = 0$ (76.6 HV at 24 mm) is improved by 33.9% compared to the weakest point of the center with $z = 2$ (57.2 Hv at 16 mm) after PWHT. The overall strength recovery is

quite significant where the induction heat has been high. This is an indication of dissolution of precipitates. The peak temperature for $z = 0$ reached 520°C in this area, reaching above SHT temperature. The simulation without the final PWHT had a RT-storage of 14 days after LPWHT. If the RT-storage was longer, natural aging may contribute to a strength increase, however not as significant as with a PWHT. Figure 6.2a and 6.2b shows the difference in hardness for the HAZ for the two simulations, $z = 2$ and $z = 0$, with no final PWHT and with a final PWHT.

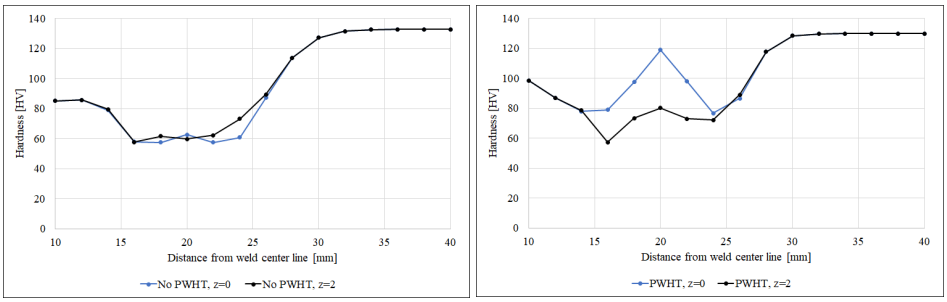

(a) **(b)**

Figure 6.2: Comparison of the predicted hardness for the HAZ for two simulations $z = 2$ and $z = 0$, with **(a)** no final PWHT and **(b)** with a final PWHT.

Figure 6.3a and 6.3b displays the difference in hardness of the HAZ for the two simulations $z = 2$ and $z = 0$, with no final PWHT and with a final PWHT described above. Note that positive values equal to $z = 0$ having a higher hardness than $z = 2$, and negative values the opposite. For the case with PWHT at the surface of the sheet, i.e. $z = 0$, the strength recovery is predicted to almost 38.7 HV more than at the center of the sheet thickness, i.e. $z = 2$, at maximum. The impact of the temperature from the applied induction is quite different in the thickness of the sheet. For natural aging of 14 days the strength has generally decreased at the surface compared to the center of the sheet thickness. The deterioration is 12.3 HV at the worst.

Figure 6.4a shows the improvement in the predicted hardness for the HAZ with no final PWHT and with a final PWHT on the surface, i.e. $z = 0$. Figure 6.4b shows the same at the center, with $z = 2$. Note that positive values equal to the PWHT having a higher hardness than without the PWHT, and negative values the opposite. This was presented in Figure 5.11 and 5.12 in chapter 5, but a more detailed comparison is made here. The improvement of predicted hardness on the surface, $z = 0$, is as high as 56.3 HV at best with the final PWHT, compared to RT-storage of 14 days. The improvement is 20.5 HV at best for the predicted hardness of the center of the thickness, $z = 2$, with a final PWHT compared to RT-storage of 14 days.

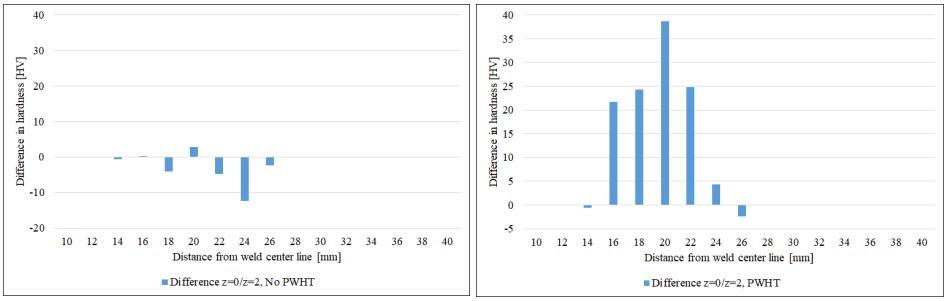

(a) **(b)**

Figure 6.3: Difference in predicted hardness for the HAZ for the two simulations $z = 2$ and $z = 0$, with **(a)** no final PWHT and **(b)** with a final PWHT. Note that positive values equal to $z = 0$ having a higher hardness than $z = 2$, and negative values the opposite.

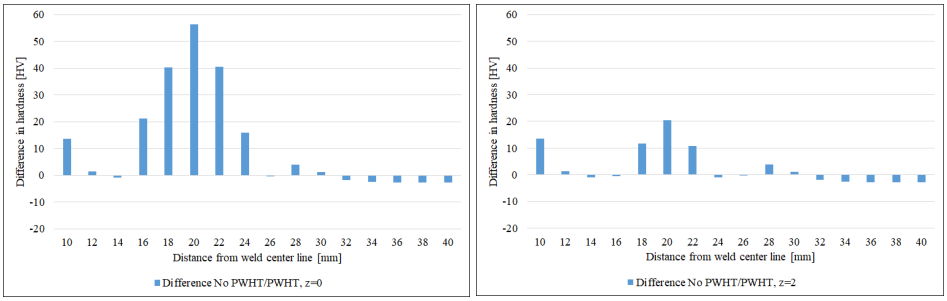

(a) **(b)**

Figure 6.4: Improvement in predicted hardness for the HAZ with no final PWHT and with a final PWHT **(a)** on the surface, $z = 0$, and **(b)** the center, $z = 2$. Note that positive values equal to the PWHT having a higher hardness than without the PWHT, and negative values the opposite.

The PWHT shows that there is possibility for strength recovery in the area affected by induction if the temperature is high enough. The simulated natural aging of 14 days RT-storage after LPWHT may not be sufficient time for a strength recovery. In general the precipitation mechanism from natural aging is quite rapid and slowly increase, meaning the most of the strength that is possible to recover with natural aging should be present.

Figure 6.5a shows the predicted hardness for the HAZ after welding, and after a LPWHT and PWHT on the surface, i.e. $z = 0$. The increase in the lowest predicted hardness in the HAZ after LPWHT and PWHT, 76.6 HV (at 24 mm from the weld center line), is 31.4 % higher than the lowest predicted hardness after welding of 58.3 HV (at 16 mm). The increase after LPWHT and PWHT (76.6 HV) is 8.7 % higher than the measured lowest value of the HAZ (70.5 HV at 15 mm from the weld center line from Figure 5.1a and 5.1b). Figure 6.5b shows the same at the center of the thickness, with $z = 2$. A decrease is

observed for the lowest hardness of the HAZ after LPWHT and PWHT compared to after welding, for the center of the thickness.

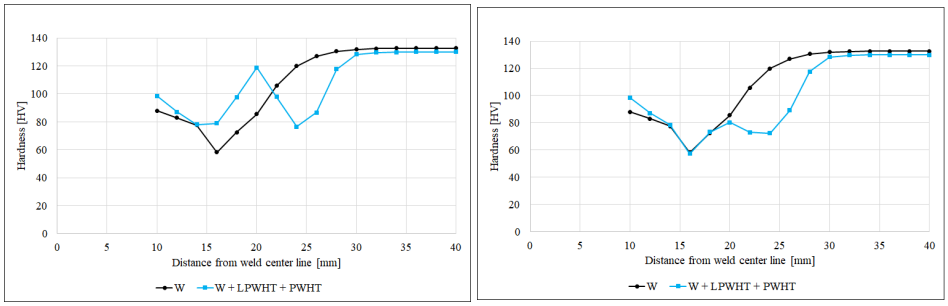

(a) **(b)**

Figure 6.5: Predicted hardness for the HAZ with after welding, and after welding, LPWHT and PWHT for **(a)** the surface, $z = 0$, and **(b)** the center, $z = 2$.

Chapter 7

Conclusion

7.1 Summary and Conclusion

The developed Weld and Induction Thermal Cycle software predicts the thermal cycles of both welding and LPWHT by induction reasonably. The analytical solutions of welding with a moving point heat source model and of induction with a stationary heat source model with a discrete distribution of partial heat sources seems to work fairly to estimate the thermal cycles during welding and LPWHT by induction. More experimental data is necessary for better predictions and fine-tuning of the developed Combined Weld and Induction Thermal Cycle software. However the software seems capable of estimating the thermal cycle during welding and LPWHT by induction reasonably at this state.

The induction apparatus used in the preceding study was found to have output power, P = 7563 W, for the described settings and conditions. With a discrete partial heat source distribution described by Equation (4.1), with $L = 40$ mm, $W = 10$ mm and $k = 0.40$, the net power input to the 6082 profile was approximated to P_{net} = 1898 W. This leaves the efficiency factor of the induction heating to η_{IND} = 0.251.

Simulations from the developed Combined Weld and Induction Thermal Cycle software indicates that induction applied for 10 seconds with the induction parameters listed above, increases the maximum temperature in the center of the induction coil at the surface of the 6082.50-T6 sheet to 520.3 °C and the temperature in the center of the sheet to 472.7 °C.

Predictions in NaMo with input from the developed Combined Weld and Induction Thermal Cycle software indicates that HAZ manipulation is possible with a LPWHT by induction. LPWHT after welding followed by a RT-storage of 14 days predicts an overall decrease of the mechanical properties in the HAZ. By applying a PWHT of 185 °C for 5.5 hours after LPWHT (instead of RT-storage), an increase in the overall mechanical properties of the HAZ was predicted at the surface, but not in the center of the thickness of the 6082.50-T6 sheet.

The biggest increase from the weakest point in the HAZ was found at the surface after a LPWHT and PWHT, with an increase of 31.4 % from the lowest predicted hardness in the HAZ after LPWHT and PWHT, 76.6 HV (at 24 mm from the weld center line), compared to the lowest predicted hardness after welding of 58.3 HV (at 16 mm). The increase after predicted LPWHT and PWHT (76.6 HV) is 8.7 % higher than the measured weakest point in the HAZ (70.5 HV at 15 mm from the weld center line).

Further analysis of the entire imprint after LPWHT by induction is needed to estimate the load bearing capacity of a welded structure after LPWHT by finite element simulations. The predictions in this thesis, does however strengthen the methodology presented in the study by Østhus et al. [9] of a globally increased load bearing capacity by LPWHT.

7.2 Recommendations for Further Work

Due to the abrupt ending of the planned experimental procedures for this thesis, the welded 6082.50-T6 sheets located at SINTEF Manufacturing AS at Raufoss await further testing. In addition to experimental testing with regard to welded components, a better understanding of the induction heating apparatus is needed. More experimental data is necessary to fine-tune the developed Weld and Induction Thermal Cycle Software. The power distribution of the induction coil and the temperature increase in the material subject to induction is critical to ensure better calibration of the software.

A more up to date Minac induction heating apparatus could decrease the uncertainty the induction heat treatment brings. SINTEF Manufacturing AS at Raufoss holds a broken Minac with a selection of different induction coils. A similar induction heating apparatus was found to be located at NTNU Gløshaugen at Bergbygget, with an unknown selection of coils. If the components match, one could have far more options of heat distribution upon induction heating. This is worth investigating.

The study by Østhus et.al [9] is a good basis for further work, including both simulations and experimental work to be done.

References

[1] J. K. Solberg. *Teknologiske metaller og legeringer*. NTNU, 2008.

[2] J. Hirsch. *Virtual fabrication of aluminum products: microstructural modeling in industrial aluminum production*. Wiley-VCH, 2006.

[3] G. Mathers. *The Welding of Aluminium and Its Alloys*. Woodhead Publishing Series in Welding and Other Joining Technologies. Elsevier Science, 2002.

[4] Ø. Grong. *Metallurgical modelling of welding*. 2nd ed. Materials modelling series. Institute of Materials, 1997.

[5] F. King. *Aluminium and its alloys*. Ellis Horwood series in metals and associated materials. Ellis Horwood, 1987.

[6] A. Hamarsnes. *Mechanical Properties of a Welded 6082 Aluminium Alloy with Local Heat Treatments*. 2019.

[7] S. B. Gjertsen. *Mechanical Properties after Welding and Post Weld Heat Treatment of a 6082 Aluminium Alloy*. 2018.

[8] J. R. Olsen. *Mechanical and Metallurgical Analysis of a Welded and Post-Weld Heat Treated 6082 Aluminium Alloy*. Unpublished. 2019.

[9] R. Østhus, O. R. Myhr, A. Nesse, A. Hamarsnes, M. Iddberg, and T. Furu. *The Use of Artificial Intelligence (AI) for Imroving Structural Properties of Welded Aluminum Extrusions*. Unpublished. 2019.

[10] N. N. Rykalin. *Berechnung der Wärmevorgänge beim Schweissen*. VEB Verlag Technik, 1957.

[11] O.R Myhr, Ø Grong, and S. .J. Andersen. "Modelling of the age hardening behaviour of Al–Mg–Si alloys". In: *Acta Materialia* 49.1 (2001), pp. 65–75.

[12] O. R. Myhr, Ø. Grong, H. G. Fjær, and C. D. Marioara. "Modelling of the microstructure and strength evolution in Al–Mg–Si alloys during multistage thermal processing". In: *Acta Materialia* 52.17 (Oct. 4, 2004), pp. 4997–5008.

[13] O. R. Myhr, Ø. Grong, and K. Pedersen. "A Combined Precipitation, Yield Strength, and Work Hardening Model for Al-Mg-Si Alloys". In: *Metallurgical and Materials Transactions A* 41.9 (2010), pp. 2276–2289.

[14] O. R. Myhr, Ø. Grong, and C. Schäfer. “An Extended Age-Hardening Model for Al-Mg-Si Alloys Incorporating the Room-Temperature Storage and Cold Deformation Process Stages”. In: *Metallurgical and Materials Transactions A* 46.12 (2015), pp. 6018–6039.

[15] Callister. *Materials science and engineering: an introduction*. In collab. with D. G. Rethwisch. 7th ed. Wiley, 2007.

[16] J.R. Davis. *Aluminum and Aluminum Alloys*. ASM specialty handbook. ASM International, 1993.

[17] Hatch, J.E. *Aluminum: Properties and Physical Metallurgy*. American Society for Metals, Aluminum Association, 1984.

[18] S. K. Fjeldbo, Y. Li, K. Marthinsen, and T. Furu. “Through-process sensitivity analysis on the effect of process variables on strength in extruded Al–Mg–Si alloys”. In: *Journal of Materials Processing Technology* 212.1 (2012), pp. 171–180.

[19] G. E. Dieter. *Mechanical metallurgy*. SI metric ed. McGraw-Hill series in materials science and engineering. McGraw-Hill, 1988.

[20] A. Malekan, M. Emamy, J. Rassizadehghani, and M. Malekan. “Effect of Isothermal Holding on Semisolid Microstructure of Al–Mg2Si Composites”. In: *ISRN Metallurgy* 2012 (2012).

[21] Ø. Grong. “Recent Advances in Solid-State Joining Of Aluminum”. In: *Welding Journal* 91 (2012), pp. 26–33.

[22] D. Rosenthal. “The Theory of Moving Sources of Heat and Its Application to Metal Treatments”. In: *Transactions of the American Society of Mechanical Engineers* 68 (1946), pp. 849–866.

[23] O.R. Myhr and Ø. Grong. “Dimensionless maps for heat flow analyses in fusion welding”. In: *Acta Metallurgica Et Materialia* 38.3 (1990), pp. 449–460.

[24] J. K. Holmen, T. Børvik, O. R. Myhr, H. G. Fjær, and O. S. Hopperstad. “Perforation of welded aluminum components: Microstructure-based modeling and experimental validation”. In: *International Journal of Impact Engineering* 84 (C 2015), pp. 96–107.

[25] T. Furu and O. R. Myhr. “Method and Apparatus for Post Weld Heat Treatment of Aluminium Alloy Components, and a Welded Aluminium Component Treated According to the Method”. Pat. WO/2019/086381. NORSK HYDRO ASA. May 9, 2019.

[26] S. Zinn. *Elements of induction heating : design, control, and applications*. Electric Power Research Institute; ASM International, 1988.

[27] *Eurocode 9: Design of aluminium structures. Part 1-1: General structural rules*. Vol. EN 1999-1-1:2007+A1. European standard. 2007.

[28] O. R. Myhr and Ø. Grong. “Novel modelling approach to optimisation of welding conditions and heat treatment schedules for age hardening Al alloys”. In: *Science and Technology of Welding and Joining* 14.4 (2009), pp. 321–332.

Appendix A

Solution Heat Treatment and Artificial Aging

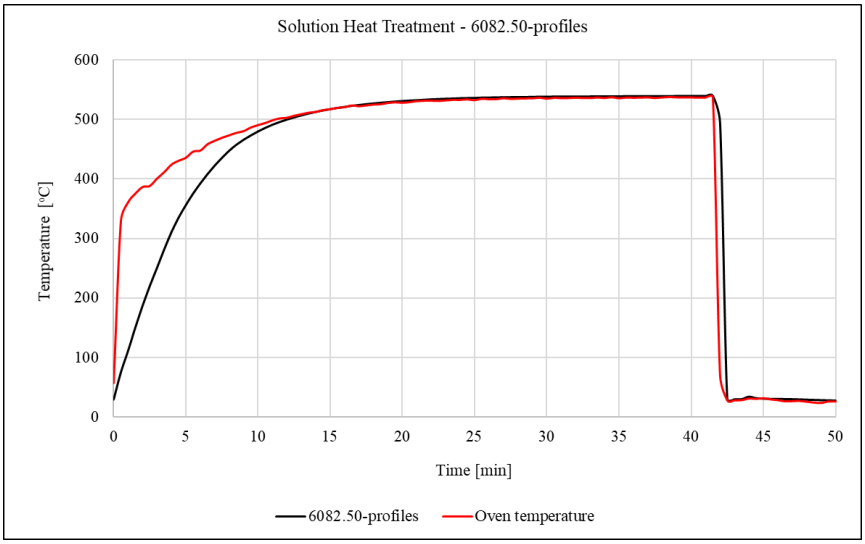

Figure A.1: Temperature logging of the solution heat treatment of the 6082.50-profiles. Logging frequency is 30 seconds.

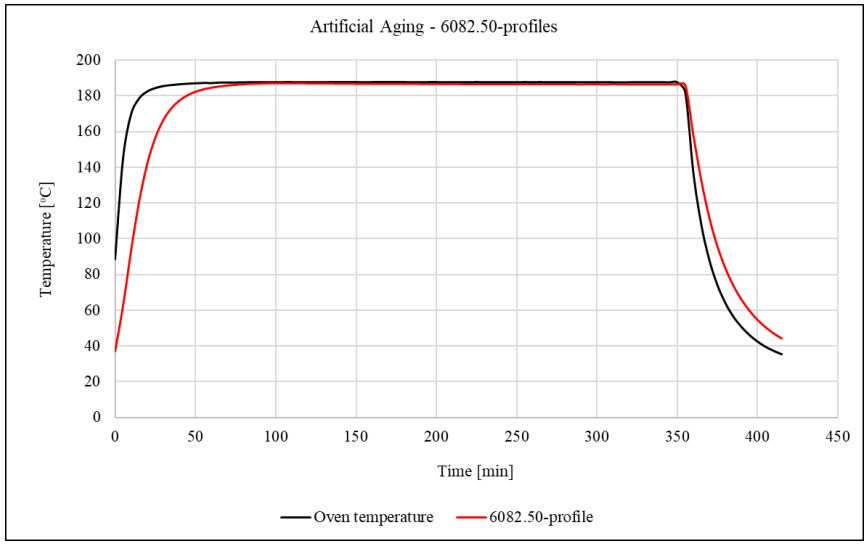

Figure A.2: Temperature logging of the artificial aging of the 6082.50-profiles. Logging frequency is 5 minutes.

Appendix B

Material Characterization

Table B.1: Grinding and polishing steps for sample preparation prior to hardness testing. *As needed until plane ground.

Step	Surface	Abrasive type	Speed [rpm]	Force per sample	Holder direction	Time [min]
Plane grinding	MD-Molto 220		300	25	>>	1*
Fine grinding	MD-Largo	DiaPro Largo 9μm	150	30	>>	4
Polish	MD-Mol	DiaPro Mol 3μm	150	25	>>	3

Appendix C

Mechanical Properties

SINTEF

19.02.20

Parameter table:

Report number	: Test for NTNU
Tester	: Erik Fredrikstad
Test standard	: NS-EN ISO 6892-1:2016 B
Req-Number	:
Cost place	:
Profile number	:
Customer	:
Profile / model type	:
Order number	:
Charge number	:

Results:

Legends	Nr	Specimen id.	S0 mm²	L0 mm	Rp 0,2 MPa	Rm MPa	Ag %	A %	HV10
	1	B4 3a 1	50,1	39,9	338	360	6,5	11,0	78
	2	B4 3a 2	49,9	39,8	338	361	6,5	11,3	78
	3	B4 3a 3	49,8	39,8	335	357	6,6	12,6	78
	4	*B4 6 1	49,6	39,7	127	197	5,9	6,1	78
	5	*B4 6 2	49,7	39,8	136	204	5,7	6,0	78
	6	*B4 6 3	49,7	39,8	137	205	5,7	6,1	78
	7	D6 4a 1	47,9	39,0	333	355	6,3	11,3	78
	8	D6 4a 2	48,1	39,1	332	355	6,4	11,6	78
	9	D6 4a 3	48,0	39,1	334	356	6,3	10,3	78
	10	*B4 3a T 1	49,9	39,8	349	363	5,0	6,8	78
	11	B4 3a T 2	49,8	39,8	351	365	5,4	10,5	78
	12	B4 3a T 3	49,9	39,8	352	366	5,7	11,0	78
	13	B4 6 T 1	49,5	39,7	155	223	9,6	18,4	78
	14	*B4 6 T 2	49,7	39,8	151	220	9,1	12,0	78
	15	B4 6 T 3	49,6	39,7	161	227	9,0	16,2	78
	16	D6 4a T 1	47,9	39,1	346	362	6,1	13,8	78
	17	*D6 4a T 2	48,0	39,1	346	361	5,5	7,2	78
	18	D6 4a T 3	48,0	39,1	344	361	6,1	12,5	78

Figure C.1: Tensile testing results of the base material of batch B (ID B4 3a) and D (ID D6 4a) for longitudinal and transverse direction relative to the extrusion direction. ID B4 6 can be overlooked. Note that * indicates fracture outside of the extensometer.

SINTEF 19.02.20

Series graph:

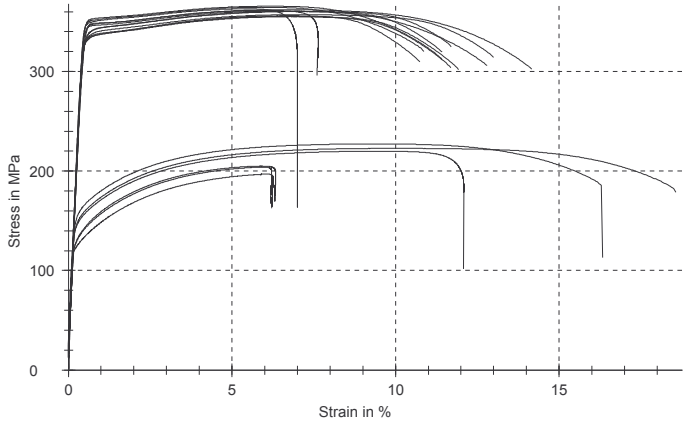

Figure C.2: Plotted tensile testing results of the base material of batch B (ID B4 3a) and D (ID D6 4a) for longitudinal and transverse direction relative to the extrusion direction. ID B4 6 can be overlooked. Note that * indicates fracture outside of the extensometer.

Appendix D

Welding

Table D.1: Extended welding parameters for the 6082.50-T6 sheets, mean values. I - welding current, U - arc voltage, WFS - wirefeed speed.

ID	Time [s]	I [A]	U [V]	WFS [mm/s]
779	42.3	239	21.9	14.1
780	24.8	239	22.1	14
781	19.4	237	22.1	14
782	42.3	239	22	14.1
783	42.3	239	22	14.1
784	42.3	240	21.8	14.1
785	42.3	239	21.8	14.1
786	42.3	238	22.2	14.1
787	42.3	238	22	14.1
788	42.3	237	22	14.1
789	42.3	237	21.9	14.1
790	42.3	238	22	14.1
791	42.3	237	22.2	14.1
792	42.3	236	22.2	14.1
793	42.3	237	21.9	14.1

Appendix E

Induction Heat Input Testing

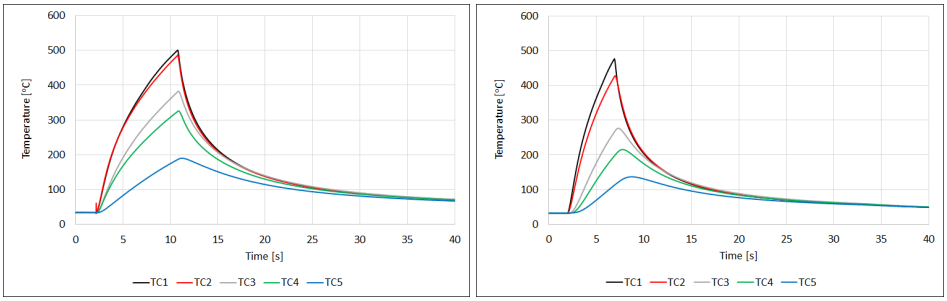

(a) **(b)**

Figure E.1: Temperature evolution during induction heat treatment of the 6082 profile, with **(a)** the induction coil parallel to the thermocouple direction (P2), and **(b)** the coil normal to the thermocouple direction (N2).

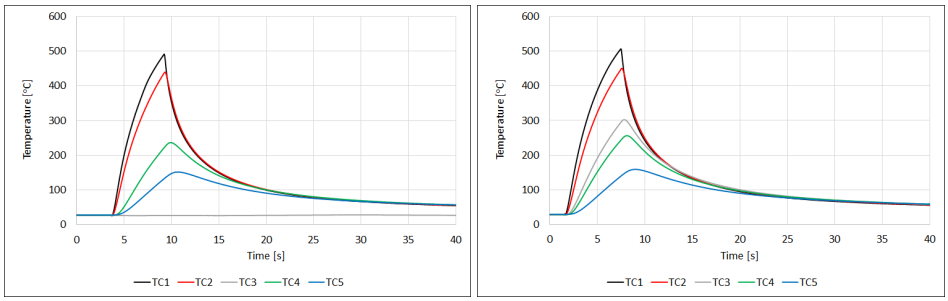

(a) **(b)**

Figure E.2: Temperature evolution during induction heat treatment of the 6082 profile, with the induction coil diagonal (45°) to the thermocouple direction, **(a)** (D1), and **(b)** (D2).

Appendix F

NaMo

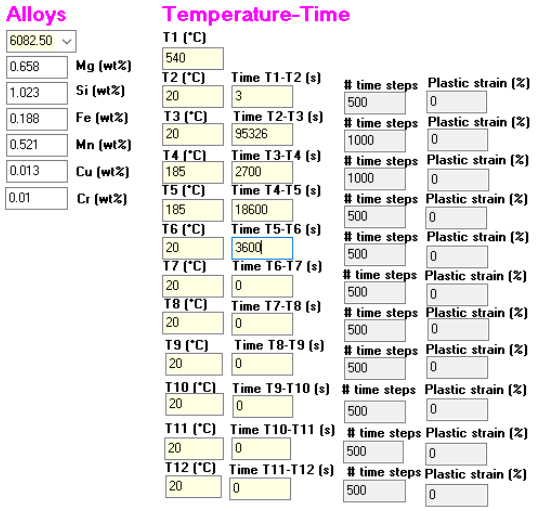

Figure F.1: NaMo input for artificial aging of the 6082.50-T6 sheets.

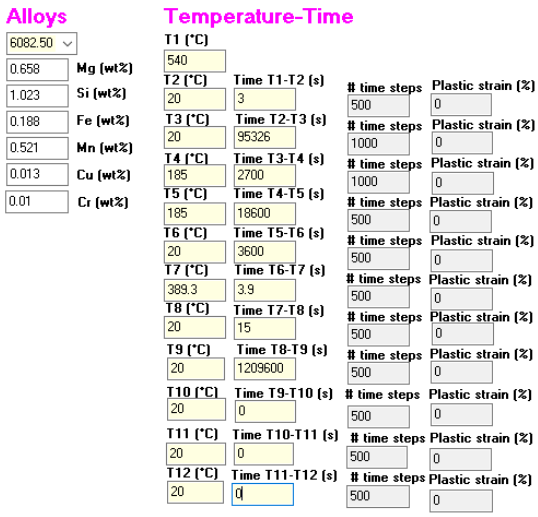

Figure F.2: Example of NaMo input for welding of the 6082.50-T6 sheets.

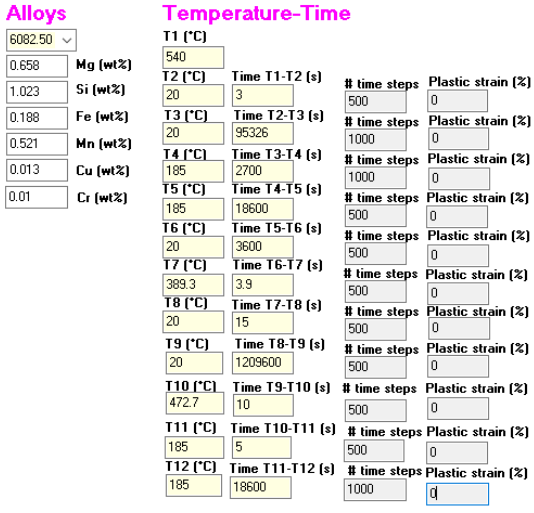

Figure F.3: Example of NaMo input for welding, LPWHT and PWHT of the 6082.50-T6 sheets.

y-position	$T_{\text{p,W}}$ [C]	$t_{\text{p,W}}$ [s]	$t_{\text{cool,W}}$ [s]	$T_{\text{p,IND}}$ [C]	$t_{\text{p,IND}}$ [s]	$t_{\text{cool,IND}}$ [s]
10	679.1	1.1	15	309.4	10.1	10
12	590.9	1.6	15	344.5	10.0	10
14	522.9	2.0	15	384.3	10.0	10
16	469.2	2.6	15	426.0	10.0	10
18	425.3	3.2	15	459.5	10.0	10
20	389.3	3.9	15	472.7	10.0	10
22	358.8	4.6	15	459.5	10.0	10
24	333.0	5.4	15	426.0	10.0	10
26	310.7	6.5	15	384.3	10.0	10
28	291.3	7.2	15	344.5	10.0	10
30	274.3	8.3	15	309.4	10.1	10
32	259.1	9.3	15	278.5	10.1	10
34	245.8	10.5	15	251.2	10.2	10
36	233.8	11.9	15	227.2	10.3	10
38	223.0	12.9	15	205.9	10.5	10
40	213.2	14.3	15	187.0	10.6	10

Table F.1: Simulated peak temperature during welding, $T_{\text{p,W}}$ and induction heating, $T_{\text{p,IND}}$, time to peak temperature, $t_{\text{p,W}}$ and $t_{\text{p,IND}}$, and cooling time, $t_{\text{cool,W}}$ and $t_{\text{cool,IND}}$. All simulations for varying y-position, and fixed $x = 0$, $z = 2$.

y-position	$T_{\text{p,W}}$ [C]	$t_{\text{p,W}}$ [s]	$t_{\text{cool,W}}$ [s]	$T_{\text{p,IND}}$ [C]	$t_{\text{p,IND}}$ [s]	$t_{\text{cool,IND}}$ [s]
10	679.1	1.1	15	309.4	10.1	10
12	590.9	1.6	15	345.4	10.0	10
14	522.9	2.0	15	388.7	10.0	10
16	469.2	2.6	15	466.3	10.0	10
18	425.3	3.2	15	497.9	10.0	10
20	389.3	3.9	15	520.0	10.0	10
22	358.8	4.6	15	497.9	10.0	10
24	333.0	5.4	15	466.3	10.0	10
26	310.7	6.5	15	388.7	10.0	10
28	291.3	7.2	15	345.4	10.0	10
30	274.3	8.3	15	309.4	10.1	10
32	259.1	9.3	15	278.5	10.1	10
34	245.8	10.5	15	251.2	10.2	10
36	233.8	11.9	15	227.2	10.3	10
38	223.0	12.9	15	205.9	10.5	10
40	213.2	14.3	15	187.0	10.6	10

Table F.2: Simulated peak temperature during welding, $T_{\text{p,W}}$ and induction heating, $T_{\text{p,IND}}$, time to peak temperature, $t_{\text{p,W}}$ and $t_{\text{p,IND}}$, and cooling time, $t_{\text{cool,W}}$ and $t_{\text{cool,IND}}$. All simulations for varying y-position, and fixed $x = 0$, $z = 0$.

Appendix G

Developed Softwares

Weld Thermal Cycle Software

```
clear
clc

%------------------------Overall ...
    menu---------------------------------------
run = menu('Weld model','Isotherms thick plate','Thermal cycle ...
    thick plate','Isotherms medium thick plate','Thermal cycle ...
    medium thick plate','Close');
%---------------------------------------------------------------------

%------------------------Run-loop-----------------------------------
while run == 1 || run == 2  || run ==3 || run == 4

%----------------------Material and welding input--------------------
if run == 1 || run == 2
    default = {'0.025','0.005','4','300','28','0.85','20'};
        var = inputdlg({'lambda [W/mmC]','rhoc [J/mm^3C]','v ...
            [mm/s]','I [A]','U [V]','ny','T0'},'',1,default);
        lambda = str2double(var(1));                        %[W/mmC]
        rhoc = str2double(var(2));                          %[J/mm^3C]
        v = str2double(var(3));                             %[mm/s]
        I = str2double(var(4));                             %[A]
        U = str2double(var(5));                             %[V]
        ny = str2double(var(6));
        T0 = str2double(var(7));                            %[C]
        a = lambda/rhoc;                                    %[mm^2/s]
elseif run == 3 || run == 4
    default = {'0.140','0.00243','10','240','22','0.7','20','4'};
        var = inputdlg({'lambda [W/mmC]','rhoc [J/mm^3C]','v ...
            [mm/s]','I [A]','U [V]','ny','T0','d'},'',1,default);
        lambda = str2double(var(1));                        %[W/mmC]
        rhoc = str2double(var(2));                          %[J/mm^3C]
        v = str2double(var(3));                             %[mm/s]
```

```
        I = str2double(var(4));                          %[A]
        U = str2double(var(5));                          %[V]
        ny = str2double(var(6));
        T0 = str2double(var(7));                         %[C]
        d = str2double(var(8));                          %[mm]
        a = lambda/rhoc;                                 %[mm^2/s]
end
    q0 = ny*I*U;                                         %[W]

%-----------------------------Calculation-----------------------------
    switch run
        case 1 %Steel - Isotherms medium thick plate
            %Dimension
            x = -100:0.5:10;                             %[mm]
            y = -20:0.5:20;                              %[mm]
            z = [0,3,6,9];                               %[mm]


            for k = 1:length(z)
                for j = 1:length(y)
                    for i = 1:length(x)
                        R(i) = sqrt((x(i))^2 + (y(j))^2 + (z(k))^2);

                        T(j,i) = T0 + (q0/(2*pi*lambda))*(1/(R(i)))*...
                        exp((-v/(2*a))*(R(i)+ x(i)));

                        if T(j,i) > 2200
                            T(j,i) = 2200;
                        end
                    end
                end

                interval = 200:200:2200;
                subplot(2,2,k)
                contourf(x,y,T,interval,'ShowText','on')
                title(sprintf('z = %0.1f mm', z(k)))
                grid on
                zlabel('Temperature [C]')
                xlabel('x-direction [mm]')
                ylabel('y-direction [mm]')

            end
        case 2 %Steel - Thermal cycle thick plate
            default2 = {'10','5'};
            var2 = ...
                inputdlg({'y-direction','z-direction'},'',1,default2);
            y2 = str2double(var2(1));                    %[mm]
            z2 = str2double(var2(2));                    %[mm]
            x = -200:0.5:10;                             %[mm]
            R2 = 0;
            T2 = 0;
            t = 0;

            for i = 1:length(x)
                R2(i) = sqrt(x(i)^2 + y2^2 + z2^2);
                T2(i) = T0 + (q0/(2*pi*lambda))*(1/R2(i))*...
                exp((-v/(2*a))*(R2(i)+x(i)));
```

```
85                  t(i) = x(i)/v;
86              end
87              Tmax = max(T2);
88              index = find(T2 == Tmax);
89              tmax = t(index);
90
91              figure;
92              plot(t,T2)
93              title(sprintf('z = %0.1f mm, y = %0.1f mm', z2, y2))
94              legend(sprintf('Peak temp = %0.1f C, time = %0.1f s', ...
                    Tmax, tmax))
95              grid on
96              ylabel('Temperature [C]')
97              xlabel('Time [s]')
98
99          case 3 %AA6xxx - Isotherms medium thick plate
100             %Dimensions
101             x = -150:0.5:10;                                %[mm]
102             y = -30:0.5:30;                                 %[mm]
103             z = [0,1/4*d,1/2*d,d];                          %[mm]
104
105             for k = 1:length(z)
106                 T = 0; %Resetting
107                 for j = 1:length(y)
108                     for i = 1:length(x)
109                         R_pos = 0; %Resetting imaginary heat sources
110                         S_pos = 0;
111                         R_neg = 0;
112                         S_neg = 0;
113                         T_new = 0;
114                         h = 0;
115                         dT = 1;
116
117                         while dT > 0.001
118
119                         %Real heat source
120                         if h == 0
121                             R_start = sqrt((x(i))^2 + (y(j))^2 + ...
                                    ((z(k))^2));
122                             S_start = ...
                                    (1/R_start)*exp(-(v/(2*a))*R_start);
123                             T_new(1) = T0 + (q0/(2*pi*lambda))*...
124                             exp((-v*x(i))/(2*a))*S_start;
125                         end
126                         %Imaginary heat sources
127                         h = h+1;
128                         R_pos(h) = sqrt((x(i))^2 + (y(j))^2 + ...
                                ((z(k)-2*h*d)^2));
129                         S_pos(h) = ...
                                (1/(R_pos(h)))*exp(-(v/(2*a))*R_pos(h));
130                         R_neg(h) = sqrt((x(i))^2 + (y(j))^2 + ...
                                ((z(k)+2*h*d)^2));
131                         S_neg(h) = ...
                                (1/(R_neg(h)))*exp(-(v/(2*a))*R_neg(h));
132                         S = S_start + sum(S_pos) + sum(S_neg);
133                         T_new(h+1) = T0 + ...
                                (q0/(2*pi*lambda))*exp((-v*x(i))/(2*a))*S;
```

```
134
135                         if T_new(h+1) < T_new(h)
136                             break
137                         end
138
139                         dT = (T_new(h+1)-T_new(h))/T_new(h);
140                         end
141
142                         T(j,i) = max(T_new);
143
144                     end
145                 end
146
147                 interval = 0:100:1000;
148                 subplot(2,2,k)
149                 contourf(x,y,T,interval,'ShowText','on')
150                 title(sprintf('z = %0.1f mm', z(k)))
151                 grid on
152                 grid minor
153                 zlabel('Temperature [C]')
154                 xlabel('x-direction [mm]')
155                 ylabel('y-direction [mm]')
156             end
157
158         case 4 %Al-Mg-Si - Thermal cycle medium thick plate
159             default2 = {'15','2'};
160             var2 = ...
                    inputdlg({'y-direction','z-direction'},'',1,default2);
161             y2 = str2double(var2(1));                    %[mm]
162             z2 = str2double(var2(2));                    %[mm]
163             x = -200:2:50;                               %[mm]
164             R2 = 0;
165             T2 = 0;
166             t = 0;
167
168             for i = 1:length(x)
169                 R_pos2 = 0; %Resetting imaginary heat sources
170                 S_pos2 = 0;
171                 R_neg2 = 0;
172                 S_neg2 = 0;
173                 T_new2 = 0;
174                 h2 = 0;
175                 dT2 = 1;
176
177                 while dT2 > 0.001
178                     %Real heat source
179                     if h2 == 0
180                         R_start2 = sqrt((x(i))^2 + (y2)^2 + ((z2)^2));
181                         S_start2 = ...
                                (1/R_start2)*exp(-(v/(2*a))*R_start2);
182                         T_new2(1) = T0 + ...
                                (q0/(2*pi*lambda))*exp((-v*x(i))/(2*a))*...
183                         S_start2;
184                     end
185                     %Imaginary heat source
186                     h2 = h2+1;
187                     R_pos2(h2) = sqrt((x(i))^2 + y2^2 + (z2-2*h2*d)^2);
```

```
188                         S_pos2(h2) = ...
                                (1/(R_pos2(h2)))*exp(-(v/(2*a))*R_pos2(h2));
189                         R_neg2(h2) = sqrt((x(i))^2 + y2^2 + (z2+2*h2*d)^2);
190                         S_neg2(h2) = ...
                                (1/(R_neg2(h2)))*exp(-(v/(2*a))*R_neg2(h2));
191                         S2 = S_start2 + sum(S_pos2)+sum(S_neg2);
192                         T_new2(h2+1) = T0 + ...
                                (q0/(2*pi*lambda))*exp((-v*x(i))/(2*a))*S2;
193
194                         if T_new2(h2+1) < T_new2(h2)
195                             break
196                         end
197
198                         dT2 = (T_new2(h2+1)-T_new2(h2))/T_new2(h2);
199                     end
200
201                     T2(i) = max(T_new2);
202                     t(i) = x(i)/v;
203
204                 end
205                     Tmax = max(T2);
206                     index = find(T2 == Tmax);
207                     tmax = t(index);
208
209                     figure;
210                     plot(t,T2)
211                     title(sprintf('z = %0.1f mm, y = %0.1f mm', z2, y2))
212                     legend(sprintf('Peak temp = %0.1f C, time = %0.1f ...
                            s', Tmax, tmax))
213                     grid on
214                     ylabel('Temperature [C]')
215                     xlabel('Time [s]')
216         end
217
218         run = menu('Weld model','Isotherms thick plate','Thermal cycle ...
                thick plate','Isotherms medium thick plate','Thermal cycle ...
                medium thick plate','Close');
219
220     end
```

Induction Thermal Cycle Software

```
clear all
clc

%-----------------------Overall menu-------------------------------
run = menu('Induction model','Isotherms and Thermal cycle','Close');
%------------------------------------------------------------------

%----------------------------Run loop------------------------------
while run == 1
%------------------------------------------------------------------
default_ex = {'1'};
var_ex = inputdlg({'Data (time) [T0]: 1 (7.49) [26.18], 2 (8.61) ...
    [34.18], 3 (5.01) [33.30], 4 (4.93) [31.82], 5 (5.51) [27.22] ...
    eller 6 (5.86) [28.82]'},'',1,default_ex);
ex_data = str2double(var_ex(1));

%Experimental data
parallel_12 = [531.2, 516.7, 403.5, 325.1, 182.3];
parallel_15 = [500.6, 486.7, 382.7, 325.9, 190.4];
normal_24 = [480.1, 435.4, 283.2, 220.8, 141.6];
normal_25 = [476.2, 427.3, 276.6, 215.4, 137.0];
diagonal_38 = [491.3 439.5, 236.5, 0, 151.6];
diagonal_39 = [506.3, 450.0, 302.3, 256.3, 159.2];

if ex_data == 1
    tc = 7.5;                                                %[s]
    T0 = 26.18;                                              %[C]
    x = 0:2:27;                                              %[mm]
    y = 0:2:27;                                              %[mm]
elseif ex_data == 2
    tc = 8.61;                                               %[s]
    T0 = 34.18;                                              %[C]
    x = 0:2:27;                                              %[mm]
    y = 0:2:27;                                               %[mm]
elseif ex_data == 3
    tc = 5.01;                                               %[s]
    T0 = 33.30;                                              %[C]
    x = 0:2:27;                                              %[mm]
    y = 0:2:27;                                              %[mm]
elseif ex_data == 4
    tc = 4.93;                                               %[s]
    T0 = 31.82;                                              %[C]
    x = 0:2:27;                                              %[mm]
    y = 0:2:27;                                              %[mm]
elseif ex_data == 5
    tc = 5.51;                                               %[s]
    T0 = 27.22;                                              %[C]
    x = 0:2:20;                                              %[mm]
    y = 0:2:20;                                              %[mm]
elseif ex_data == 6
    tc = 5.86;                                               %[s]
    T0 = 28.82;                                              %[C]
    x = 0:2:20;                                              %[mm]
    y = 0:2:20;                                              %[mm]
```

```
53  end
54
55  parallel_coord = [0,4,9,16,27];
56  normal_coord = [0,4,9,16,27];
57  diagonal_coord = ...
        [0,sqrt((4^2)/2),sqrt((9^2)/2),sqrt((16^2)/2),sqrt((27^2)/2)];
58  O = zeros(5,1);
59
60  %------------------------Induction Input--------------------------
61  default = {'0.140','0.00243','1900','1','3.6','0','0','0'};
62  var = inputdlg({'lambda [W/mmC]','rhoc [J/mm^3C]','P [W]','ny','d ...
        [mm]','x [mm]', 'y [mm]','z [mm]'},'',1,default);
63  lambda = str2double(var(1));                                    %[W/mmC]
64  rhoc = str2double(var(2));                                      %[J/mm^3C]
65  P = str2double(var(3));                                         %[W]
66  ny = str2double(var(4));
67  d = str2double(var(5));                                         %[mm]
68  x_tc = str2double(var(6));                                      %[mm]
69  y_tc = str2double(var(7));                                      %[mm]
70  z_tc = str2double(var(8));                                      %[mm]
71
72
73  a = lambda/rhoc;                                                %[mm^2/s]
74  dt = 0.001;                                                     %[s]
75  t = 0:dt:20;                                                    %[s]
76  tsink = 0:dt:(t(end)-tc+dt);                                    %[s]
77  z = z_tc;                                                       %[mm]
78
79  Tx = repmat(T0,length(y),length(x));
80  T(1) = T0;                                                      %[C]
81  T_ind = repmat(T0,length(t),1);
82  T_nn = repmat(T0,length(t),(length(x)*length(y)));
83  xy_pos = ones(length(x),length(y));
84  %----------------------------------------------------------------
85
86  %-----------------------Heat source distribution-----------------
87  x_mark = -20:1:20; %[mm]  %Coil, x-dimension
88  y_mark = -5:1:5; %[mm]    %Coil, y-dimension
89  z_mark = 0;
90
91
92  w = 10;
93  kw = 0.40*w;
94  l = 40;
95  kl = 0.40*l;
96
97  NN = length(x_mark)*length(y_mark);
98  dP1 = 0;
99
100 for jj = 1:length(y_mark)
101     for ii = 1:length(x_mark)
102         dP1(jj,ii) = exp(-(x_mark(ii)/kl)^(2)-(y_mark(jj)/kw)^(2));
103     end
104 end
105
106 S = sum(sum(dP1));
107 dP = (P*ny/S).*dP1;
```

```
S1 = sum(sum(dP));
%-------------------------------------------------------------------

h = waitbar(0,'Please wait...');

%----------------------Calculation of temperature-------------------
for jj = 1:length(y_mark)
for ii = 1:length(x_mark)
    nn = 1;
    for j = 1:length(y)
        for i = 1:length(x)
            %Resetting
            dT = 0;
            dTsink = 0;
            T = T0;
            for n = 2:length(t)
                %Resetting imaginary heat sources
                S_img = 0;
                m = 0;
                d_img = 1;
                img = 0;
                S_imgsink = 0;
                msink = 0;
                d_imgsink = 1;
                imgsink = 0;

                while d_img > 0.001 %Imaginary heat sources
                    if m == 0 %Real heat source
                        img(m+1) = (exp(-((z-2*m*d)^2)/(4*a*t(n))));
                    end
                    m = m+1;
                    img(m+1) = (exp(-((z-2*m*d)^2)/(4*a*t(n)))+...
                    exp(-((z+2*m*d)^2)/(4*a*t(n))));
                    d_img = (img(m+1)/img(m));
                end

                if t(n) > tc %Heatsinks when t>tc
                while d_imgsink > 0.001 %Heatsinks imaginary heat ...
                    sources
                    if msink == 0
                        imgsink(msink+1) = (exp(-((z-2*msink*d)^2)/...
                        (4*a*tsink(n-(tc/dt)+1))));
                    end
                    msink = msink+1;
                    imgsink(msink+1) = (exp(-((z-2*msink*d)^2)/...
                    (4*a*tsink(n-(tc/dt)+1)))+...
                    exp(-((z+2*msink*d)^2)/(4*a*tsink(n-(tc/dt)+1))));
                    d_imgsink = (imgsink(msink+1)/imgsink(msink));
                end
                end

                S_img = sum(img);
                S_imgsink = sum(imgsink);

                if t(n) > tc
                    dTsink(n) = -(dP(jj,ii)/...
                    (rhoc*(4*pi*a*tsink(n-(tc/dt)+1))^(3/2)))*...
```

```
164                     (exp(-(((x(i)-x_mark(ii))^2)+...
165                     ((y(j)-y_mark(jj))^2))/...
166                     (4*a*tsink(n-(tc/dt)+1))))*S_imgsink*dt;
167                 else
168                         dTsink(n) = 0;
169                 end
170
171                 dT(n) = (dP(jj,ii)/(rhoc*(4*pi*a*t(n))^(3/2)))*...
172                 (exp(-(((x(i)-x_mark(ii))^2)+((y(j)-y_mark(jj))^2))/...
173                 (4*a*t(n))))*S_img*dt;
174
175                 if x(i) == x_tc && y(j) == y_tc && z == z_tc
176                     T_ind(n) = T_ind(n) + sum(dT) + sum(dTsink);
177                     o = nn;
178                 end
179
180                 T_nn(n,nn) = T_nn(n,nn) + sum(dT) + sum(dTsink);
181                 xy_pos(j,i) = nn;
182             end
183
184             index = find(t == tc);
185             Tx(j,i) = Tx(j,i) + sum(dT(1:index));
186             nn = nn + 1;
187         end
188     end
189 end
190     waitbar(jj/length(y_mark),h, sprintf('Progress: %.0f percent', ...
        jj/length(y_mark)*100))
191 end
192
193
194 %----------------------------Plotting--------------------------------
195
196         %Heat distribution
197         figure;
198         contourf(x_mark,y_mark,dP,'ShowText','on')
199         title(sprintf('Heatsource distribution'))
200         grid on
201         grid minor
202         zlabel('dP-distribution')
203         xlabel('x^,-direction [mm]')
204         ylabel('y^,-direction [mm]')
205
206         %Isotherms
207         interval = 0:100:1000;
208         figure;
209         Tx_max = max(max(Tx));
210         contourf(x,y,Tx, interval,'ShowText','on')
211         title(sprintf('z = %0.1f mm', z))
212         legend(sprintf('Peak temp = %0.1f C', Tx_max))
213         grid on
214         grid minor
215         zlabel('Temperature [C]')
216         xlabel('x-direction [mm]')
217         ylabel('y-direction [mm]')
218
219         %Experimental values
```

```
220         hold on
221         if ex_data == 1
222         plot3(parallel_coord, ...
                O,parallel_12,'d','color','k','markersize',5)
223         strValues1 = ...
                strtrim(cellstr(num2str([parallel_12(:)],'(%0.f)')));
224         text(parallel_coord,O,strValues1,'VerticalAlignment','bottom');
225         elseif ex_data == 2
226         plot3(parallel_coord, O, ...
                parallel_15,'d','color','k','markersize',5)
227         strValues2 = ...
                strtrim(cellstr(num2str([parallel_15(:)],'(%0.f)')));
228         text(parallel_coord,O,strValues2,'VerticalAlignment','bottom');
229         elseif ex_data == 3
230         plot3(O, normal_coord, ...
                normal_24,'d','color','k','markersize',5)
231         strValues3 = ...
                strtrim(cellstr(num2str([normal_24(:)],'(%0.f)')));
232         text(O,normal_coord,strValues3,'VerticalAlignment','bottom');
233         elseif ex_data == 4
234         plot3(O, normal_coord, ...
                normal_25,'d','color','k','markersize',5)
235         strValues4 = ...
                strtrim(cellstr(num2str([normal_25(:)],'(%0.f)')));
236         text(O,normal_coord,strValues4,'VerticalAlignment','bottom');
237         elseif ex_data == 5
238         plot3(diagonal_coord, ...
                diagonal_coord,diagonal_38,'d','color','k','markersize',5)
239         strValues5 = ...
                strtrim(cellstr(num2str([diagonal_38(:)],'(%0.f)')));
240         text(diagonal_coord, ...
                diagonal_coord,strValues5,'VerticalAlignment','bottom');
241         elseif ex_data == 6
242         plot3(diagonal_coord, diagonal_coord, ...
                diagonal_39,'d','color','k','markersize',5)
243         strValues6 = ...
                strtrim(cellstr(num2str([diagonal_39(:)],'(%0.f)')));
244         text(diagonal_coord, ...
                diagonal_coord,strValues6,'VerticalAlignment','bottom');
245         end
246
247         %Thermal cycle
248         figure;
249         T_indmax = max(T_ind);
250         index = find(T_indmax == T_ind);
251         tmax = t(index);
252         plot(t,T_ind)
253         title(sprintf('x = %0.1f mm, y = %0.1f mm, z = %0.1f mm', ...
                x_tc, y_tc, z_tc))
254         legend(sprintf('Peak temp = %0.1f C, time = %0.1f s', ...
                T_indmax, tmax))
255         grid on
256         ylabel('Temperature [C]')
257         xlabel('Time [s]')
258
259 run = menu('Induction model','Isotherms and Thermal cycle','Close');
260
```

```
261 end
262 close(h)
```

Combined Weld and Induction Thermal Cycle Software

```
clear all
clc

%------------------------Overall menu-------------------------------
run = menu('Run simulation','Welding','Welding and Induction','Close');
%-------------------------------------------------------------------

%------------------------Run-loop-----------------------------------
while run == 1 || run == 2
%-------------------------------------------------------------------

%---------------Material Input--------------------------------------
def1 = {'0.140','0.00243','20','3.6','0','20','0'};
dlg_title = 'Input material properties';
var1 = inputdlg({'lambda [W/mmC]','rhoc [J/mm^3C]','T0 [C]','d ...
    [mm]','x [mm]', 'y [mm]','z [mm]'},dlg_title,1,def1);
lambda = str2double(var1(1));                                    % ...
    [W/mmC]
rhoc = str2double(var1(2));                                      % ...
    [J/mm^3C]
T0 = str2double(var1(3));                                        % [C]
d = str2double(var1(4));                                         % [mm]
x = str2double(var1(5));                                         % [mm]
y = str2double(var1(6));                                         % [mm]
z = str2double(var1(7));                                         % [mm]
%-------------------------------------------------------------------

if run == 1
%---------------Weld Input------------------------------------------
def2 = {'10','240','22','0.6','120'};
var2 = inputdlg({'v_weld [mm/s]','I_weld [A]','U_weld ...
    [V]','Eff_arc','t_RTstore [s]'},'',1,def2);
v_weld = str2double(var2(1));                                    % ...
    [mm/s]
I_weld = str2double(var2(2));                                    % [A]
U_weld = str2double(var2(3));                                    % [V]
Eff_arc = str2double(var2(4));
t_RTstore = str2double(var2(5));                                 % [s]

elseif run == 2
%---------------Weld and Induction Input----------------------------
def2 = {'10','240','22','0.6','120','7563','0.251','10','0','20'};
var2 = inputdlg({'v_weld [mm/s]','I_weld [A]','U_weld ...
    [V]','Eff_arc','t_RTstore [s]','P_ind [W]','Eff_ind','t_c_ind ...
    [s]','x_ind_center [mm]', 'y_ind_center [mm]'},'',1,def2);
v_weld = str2double(var2(1));                                    % ...
    [mm/s]
I_weld = str2double(var2(2));                                    % [A]
U_weld = str2double(var2(3));                                    % [V]
Eff_arc = str2double(var2(4));
t_RTstore = str2double(var2(5));                                 % [s]
P_ind = str2double(var2(6));                                     % ...
    [W/mmC]
Eff_ind = str2double(var2(7));                                   % ...
```

```
        [J/mm^3C]
t_c_ind = str2double(var2(8));                                          % [W]
x_ind_center = str2double(var2(9));                                     %[mm]
y_ind_center = str2double(var2(10));                                    %[mm]
%-------------------------------------------------------------------------
end

t_tot = 0;
%--------------------------Calculation Weld-------------------------
a = lambda/rhoc;                                                        % ...
    [mm^2/s]
q0_weld = Eff_arc*I_weld*U_weld;                                        % [W]
dt_weld = 0.01;
xdiff = v_weld*dt_weld;

R2 = 0;
T2 = 0;
t_weld = 0;
t_weld2 = 0;

i_weld = 0;
x_weld(1) = 50;

t_RTstore2 = x_weld(1)*dt_weld*v_weld + t_RTstore;

while t_weld2(end) ≤ t_RTstore2
    i_weld = i_weld + 1;
    x_weld(i_weld+1) = x_weld(i_weld) - xdiff;

    R_pos2 = 0; % Resetting imaginary heat sources
    S_pos2 = 0;
    R_neg2 = 0;
    S_neg2 = 0;
    T_new2 = 0;
    h2 = 0;
    dT2 = 1; % Variabel to enter the calculation of imaginary heat ...
        sources

    while dT2 > 0.001 % Convergence when dT2 ≤ 0.001
        % First term in the series is the real heat sourcce
        if h2 == 0
            R_start2 = sqrt((x_weld(i_weld))^2 + (y)^2 + ((z)^2));
            S_start2 = (1/R_start2)*exp(-(v_weld/(2*a))*R_start2);
            T_new2(1) = T0 + (q0_weld/(2*pi*lambda))*...
            exp((-v_weld*x_weld(i_weld))/(2*a))*S_start2;
        end
        % The rest of the posistive and negative terms in the series
        h2 = h2+1;
        R_pos2(h2) = sqrt((x_weld(i_weld))^2 + y^2 + (z-2*h2*d)^2);
        S_pos2(h2) = (1/(R_pos2(h2)))*exp(-(v_weld/(2*a))*R_pos2(h2));
        R_neg2(h2) = sqrt((x_weld(i_weld))^2 + y^2 + (z+2*h2*d)^2);
        S_neg2(h2) = (1/(R_neg2(h2)))*exp(-(v_weld/(2*a))*R_neg2(h2));
        S2 = S_start2 + sum(S_pos2) + sum(S_neg2);
        T_new2(h2+1) = T0 + (q0_weld/(2*pi*lambda))*...
        exp((-v_weld*x_weld(i_weld))/(2*a))*S2;

        if T_new2(h2+1) < T_new2(h2)
```

```
100             break
101         end
102
103         dT2 = (T_new2(h2+1)-T_new2(h2))/T_new2(h2);
104     end
105
106     T2(i_weld) = max(T_new2); % Converging term is used in T-t
107     t_weld(i_weld) = x_weld(i_weld)/v_weld;
108 %     index_t_weld = find(x_weld==0);  % M   fikse  s   den finner x=0
109 %     x_weld1 = x_weld(index_t_weld-1);
110     t_weld2(i_weld+1) = t_weld2(i_weld) + dt_weld;
111
112 end
113 %-------------------------------------------------------------------
114
115 if run == 2
116
117 % Wait bar
118 h_wait = waitbar(0,'Please wait...');
119
120 %-------------------------Calculation Induction----------------------
121 dt_ind = 0.001;                                                    % [s]
122 T0_ind = T0; % Or T2(end) to continue directly from the welding % [s]
123 T_ind(1) = T0_ind;                                                 % [C]
124
125 % Predefined vectors
126 t_ind = 0:dt_ind:10;                                               % [s]
127 t_ind_sink = 0:dt_ind:(t_ind(end)-t_c_ind+dt_ind);                 % [s]
128 T_nn_ind = repmat(T0_ind,(length(x)*length(y)),length(t_ind));  % [C]
129 %-------------------------------------------------------------------
130
131 %-----------------------Heat source distribution--------------------
132 % x-position and dimension of the coil
133 x_mark = -20:1:20;                                                 % [mm]
134 % y-position of the coil
135 y_mark = (-5+y_ind_center):1:(5+y_ind_center);                     % [mm]
136 %y-dimension of the coil
137 y_mark_heatdistr = -5:1:5;                                         % [mm]
138 z_mark = 0;                                                        % [mm]
139
140 w = 10;                                                            % [mm]
141 kw = 0.40*w; % Normal distribution variabel in the x-dimension
142 l = 40;                                                            % [mm]
143 kl = 0.40*l; % Normal distribution variabel in the y-dimension
144
145 NN = length(x_mark)*length(y_mark);  % Total number of partial heat ...
        sources
146 P_i_intitial = 0;                                                  % [W]
147
148 % Normal ditribution of partial heat sources
149 for jj_ind = 1:length(y_mark_heatdistr)
150     for ii_ind = 1:length(x_mark)
151         P_i_intitial(jj_ind,ii_ind) = ...
                exp(-(x_mark(ii_ind)/kl)^2-(y_mark_heatdistr(jj_ind)/kw)^2);
152     end
153 end
154
```

```
155 % Adjusting intensity of partia heat sources so sum(P_i)=P
156 SumP_ind = sum(sum(P_i_intitial));                                  % [W]
157 P_i = (P_ind*Eff_ind/SumP_ind).*P_i_intitial;                       % [W]
158 SumP_ind1 = sum(sum(P_i));                                          % [W]
159 %-------------------------------------------------------------------------
160
161 %------------------------Calculation Induction-------------------------
162 for jj_ind = 1:length(y_mark)
163 for ii_ind = 1:length(x_mark)
164     nn_ind = 1; % Resetting counting variable
165     for j_ind = 1:length(y)
166         for i_ind = 1:length(x)
167             % Resetting variables for each point (x,y)
168             dT_ind = 0;
169             dT_ind_sink = 0;
170             T_ind = T0_ind;
171             for n_ind = 2:length(t_ind)
172                 % Resetting variables for imaginary heat sources
173                 Sum_img_ind = 0;
174                 img_ind = 0;
175                 m_ind = 0; % Resetting counting variable
176                 diff_img_ind = 1; % Variable to enter calculation ...
                        of imaginary heat sources
177
178                 % Resetting variables for imaginary heat sources ...
                        heatsinks
179                 Sum_imgsink_ind = 0;
180                 imgsink_ind = 0;
181                 msink_ind = 0; % Resetting counting variable
182                 diff_imgsink_ind = 1; % Variable to enter ...
                        calculation of imaginary heat sources for ...
                        heatsinks
183
184                 while diff_img_ind > 0.001 % Convergence when ...
                        diff_img_ind ≤ 0.001
185                     % First term in the series i.e. real heat source
186                     if m_ind == 0
187                         img_ind(m_ind+1) = (exp(-((z-2*m_ind*d)^2)/...
188                         (4*a*t_ind(n_ind))));
189                     end
190                     % The rest of the positive and negative terms ...
                            in the series i.e. imaginary heat source
191                     m_ind = m_ind+1;
192                     img_ind(m_ind+1) = ...
                            (exp(-((z-2*m_ind*d)^2)/(4*a*t_ind(n_ind)))+...
193                     exp(-((z+2*m_ind*d)^2)/(4*a*t_ind(n_ind))));
194                     diff_img_ind = (img_ind(m_ind+1)/img_ind(m_ind));
195                 end
196
197                 % Turning on heatsinks when t > t_c_ind
198                 if t_ind(n_ind) ≥ t_c_ind
199                 while diff_imgsink_ind > 0.001 % Convergence when ...
                        diff_imgsink_ind ≤ 0.001
200                     % First term in the series i.e. real heat ...
                            source for heatsinks
201                     if msink_ind == 0
202                         imgsink_ind(msink_ind+1) = ...
```

```
                                (exp(-((z-2*msink_ind*d)^2)/...
203                         (4*a*t_ind_sink(n_ind-(t_c_ind/dt_ind)+1))));
204                     end
205                     % The rest of the positive and negative terms ...
                            in the series i.e. imaginary heat source
206                     msink_ind = msink_ind+1;
207                     imgsink_ind(msink_ind+1) = ...
                            (exp(-((z-2*msink_ind*d)^2)/...
208                     (4*a*t_ind_sink(n_ind-(t_c_ind/dt_ind)+1)))+...
209                     exp(-((z+2*msink_ind*d)^2)/...
210                     (4*a*t_ind_sink(n_ind-(t_c_ind/dt_ind)+1))));
211
212                     diff_imgsink_ind = (imgsink_ind(msink_ind+1)/...
213                     imgsink_ind(msink_ind));
214                 end
215                 end
216
217                 % Summing all contributions from imaginary heat sources
218                 Sum_img_ind = sum(img_ind);
219                 Sum_imgsink_ind = sum(imgsink_ind);
220
221                 % Change in temperature from heatsinks if t > t_c_ind
222                 if t_ind(n_ind) ≥ t_c_ind
223                     dT_ind_sink(n_ind) = -(P_i(jj_ind,ii_ind)/...
224                     (rhoc*(4*pi*a*t_ind_sink(n_ind-...
225                     (t_c_ind/dt_ind)+1))^(3/2)))*...
226                     (exp(-(((x(i_ind)-x_mark(ii_ind))^2)+...
227                     ((y(j_ind)-y_mark(jj_ind))^2))/...
228                     (4*a*t_ind_sink(n_ind-(t_c_ind/dt_ind)+1))))*...
229                     Sum_imgsink_ind*dt_ind;
230                 else
231                     dT_ind_sink(n_ind) = 0;
232                 end
233
234                 % Change in temperature
235                 dT_ind(n_ind) = ...
                        (P_i(jj_ind,ii_ind)/(rhoc*(4*pi*a*t_ind(n_ind))^...
236                 (3/2)))*(exp(-(((x(i_ind)-x_mark(ii_ind))^2)+...
237                 ((y(j_ind)-y_mark(jj_ind))^2))/...
238                 (4*a*t_ind(n_ind))))*Sum_img_ind*dt_ind;
239
240                 % Temperature as a function of time in each point (x,y)
241                 T_nn_ind(nn_ind,n_ind) = T_nn_ind(nn_ind,n_ind) + ...
                        sum(dT_ind) + sum(dT_ind_sink);
242             end
243         end
244     end
245 end
246     waitbar(jj_ind/length(y_mark),h_wait, sprintf('Progress: %.0f ...
            percent', jj_ind/length(y_mark)*100))
247 end
248
249 % Total temperature-time for welding and induction
250 t_tot = [-t_weld, (t_ind - t_weld(end))];
251 T_tot = [T2, T_nn_ind];
252
253 close(h_wait)
```

```
254
255 end
256
257 %-----------------------Plotting ...
        results----------------------------------
258 %Weld thermal cycle
259 figure;
260 Tmax_weld = max(T2);
261 index_weld = find(T2 == Tmax_weld);
262 tmax_weld = -t_weld(index_weld);
263 plot(-t_weld,T2)
264 title(sprintf('y = %0.1f mm, z = %0.1f mm', y, z))
265 legend(sprintf('Peak temp = %0.1f C, time = %0.1f s', Tmax_weld, ...
        tmax_weld))
266 grid on
267 ylabel('Temperature [C]')
268 xlabel('Time [s]')
269
270 if run == 2
271 %Induction thermal cycle
272 figure;
273 Tmax_ind = max(T_nn_ind);
274 index1 = find(Tmax_ind == T_nn_ind);
275 tmax_ind = t_ind(index1);
276 plot(t_ind,T_nn_ind)
277 title(sprintf('x = %0.1f mm, y = %0.1f mm, z = %0.1f mm', x, y, z))
278 legend(sprintf('Peak temp = %0.1f C, time = %0.1f s', Tmax_ind, ...
        tmax_ind))
279 grid on
280 ylabel('Temperature [C]')
281 xlabel('Time [s]')
282
283 %Total thermal cycle
284 figure;
285 plot(t_tot,T_tot)
286 title(sprintf('x = %0.1f mm, y = %0.1f mm, z = %0.1f mm', x, y, z))
287 legend(sprintf('Weld peak temp = %0.1f C, time = %0.1f s, Induction ...
        peak temp = %0.1f C, time = %0.1f s',Tmax_weld, tmax_weld, ...
        Tmax_ind, tmax_ind))
288 grid on
289 ylabel('Temperature [C]')
290 xlabel('Time [s]')
291 end
292
293 run = menu('Run simulation','Welding','Welding and Induction','Close');
294
295 end
```